SIAM J. IMAGING SCIENCES
Vol. 12, No. 1, pp. 492–520

Whole Brain Susceptibility Mapping Using Harmonic Incompatibility Removal*

Chenglong Bao†, Jae Kyu Choi‡, and Bin Dong§

Abstract. Quantitative susceptibility mapping (QSM) uses the phase data in magnetic resonance signals to visualize a three-dimensional susceptibility distribution by solving the magnetic field to susceptibility inverse problem. Due to the presence of zeros of the integration kernel in the frequency domain, QSM is an ill-posed inverse problem. Although numerous regularization-based models have been proposed to overcome this problem, incompatibility in the field data, which leads to deterioration of the recovery, has not received enough attention. In this paper, we show that the data acquisition process of QSM inherently generates a harmonic incompatibility in the measured local field. Based on this discovery, we propose a novel regularization-based susceptibility reconstruction model with an additional sparsity-based regularization term on the harmonic incompatibility. Numerical experiments show that the proposed method achieves better performance than existing approaches.

Key words. quantitative susceptibility mapping, magnetic resonance imaging, deconvolution, partial differential equation, harmonic incompatibility removal, two system regularization

AMS subject classifications. 35R30, 42B20, 45E10, 65K10, 68U10, 90C90, 92C55

DOI. 10.1137/18M1191452

1. Introduction.

Quantitative susceptibility mapping (QSM) [13] is a novel imaging technique that visualizes the magnetic susceptibility distribution from the measured field data associated with magnetization $\mathbf{M} = (M_1, M_2, M_3)$ induced in the body by an MR scanner. The magnetic susceptibility χ is an intrinsic property of the material which relates $\mathbf{M}$ and the magnetic field $\mathbf{H} = (H_1, H_2, H_3)$ through $\mathbf{M} = \chi\mathbf{H}$ [45]. As physiological and/or pathological processes alter tissues' magnetic susceptibilities, QSM has been widely applied in biomedical image analysis [45]. Applications include demyelination, inflammation, and iron overload in multiple sclerosis [8]; neurodegeneration and iron overload in Alzheimer's disease [1]; Huntington's disease [50]; changes in metabolic oxygen consumption [25]; hemorrhage, including microhemorrhage and blood degradation [28]; bone mineralization [14]; and drug delivery using magnetic nanocarriers [34].

QSM uses the phase data of a complex gradient echo (GRE) signal as the phase linearly increases with respect to the field perturbation induced by the magnetic susceptibility distribution in an MR scanner [52]. More concretely, assume that an object is placed in an MR scanner with the main static magnetic field $\mathbf{B}_0 = (0, 0, B_0)$, where B_0 is a positive constant.

*Received by the editors May 31, 2018; accepted for publication (in revised form) December 26, 2018; published electronically February 28, 2019.
http://www.siam.org/journals/siims/12-1/M119145.html
Funding: The research of the third author was supported by NSFC grant 91530321.
†Yau Mathematical Sciences Center, Tsinghua University, Beijing, 100084 China (clbao@mail.tsinghua.edu.cn).
‡Corresponding author. School of Mathematical Sciences, Tongji University, Shanghai, 200092 China (jaycjk@tongji.edu.cn).
§Beijing International Center for Mathematical Research and Laboratory for Biomedical Image Analysis, Beijing Institute of Big Data Research, Peking University, Beijing, 100871 China (dongbin@math.pku.edu.cn).

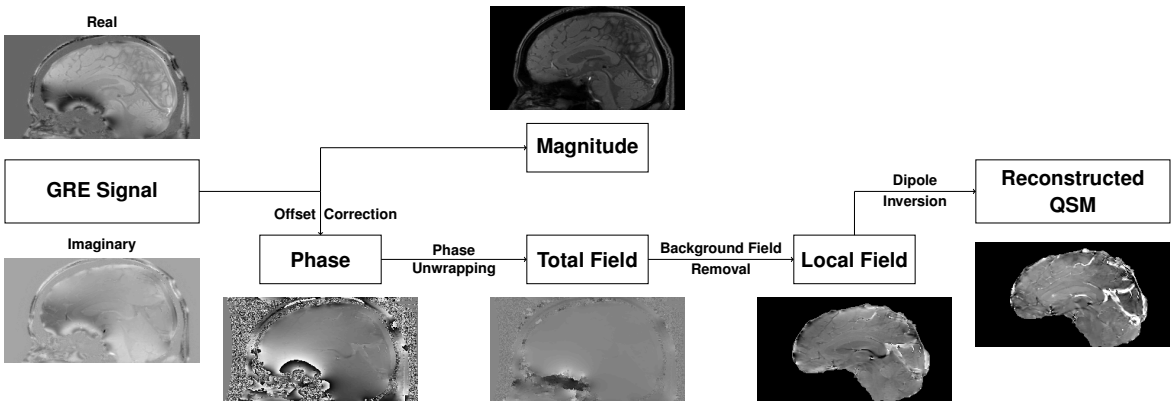

Figure 1. *Schematic diagram of QSM reconstruction process.*

Then, for any $\boldsymbol{x} \in \mathbb{R}^3$, the observed complex GRE signal $I(\boldsymbol{x}, TE)$ at an echo time TEsec is modeled as

$$I(\boldsymbol{x}, TE) = m(\boldsymbol{x}) \exp\left\{-i\left(b(\boldsymbol{x})\omega_0 B_0 TE + \theta_0(\boldsymbol{x})\right)\right\}, \tag{1.1}$$

where $\omega_0 = 42.577$MHz/T is the proton gyromagnetic ratio, b is the total field induced by the susceptibility distribution in an MR scanner, and θ_0 is the coil sensitivity–dependent phase offset. The magnitude image $m(\boldsymbol{x})$ in (1.1) is proportional to the proton density [52], and the phase $\theta(\boldsymbol{x})$ in $I(\boldsymbol{x}, TE)$ is written as

$$\theta(\boldsymbol{x}) = b(\boldsymbol{x})\omega_0 B_0 TE + \theta_0(\boldsymbol{x}). \tag{1.2}$$

Based on the observations $\theta(\boldsymbol{x})$, QSM aims at visualizing the susceptibility distribution $\chi(\boldsymbol{x})$ in the region of interest (ROI) Ω which occupies the water and brain tissues. Note that the ROI Ω can be readily determined by $I(\boldsymbol{x}, TE)$ (and thus by $m(\boldsymbol{x})$) as $m(\boldsymbol{x}) = |I(\boldsymbol{x}, TE)| \approx 0$ whenever $\boldsymbol{x} \notin \Omega$ [30, 44, 52]. The standard QSM consists of the following four steps: offset correction, phase unwrapping, background field removal, and dipole inversion (see Figure 1 for the overview of the process). The first three steps extract the local field b_l that is contained in the total field b: the offset correction removes/corrects $\theta_0(\boldsymbol{x})$ from $\theta(\boldsymbol{x})$ to obtain $b(\boldsymbol{x})\omega_0 B_0 TE$ (the offset corrected phase) lying in $(-\pi, \pi]$; the phase unwrapping removes the artificial jumps in the offset corrected phase when estimating the total field b; the background field removal eliminates the field induced by the susceptibility outside Ω such as skulls and nasal cavities. Interested readers may refer to [24, 44, 52] and references therein for more details.

Given the local field b_l, the dipole inversion recovers the susceptibility distribution χ in Ω by solving the following convolution relation [31, 32, 33]:

$$b_l(\boldsymbol{x}) = \mathrm{pv} \int_\Omega d(\boldsymbol{x} - \boldsymbol{y})\chi(\boldsymbol{y})\mathrm{d}\boldsymbol{y}, \tag{1.3}$$

where pv denotes the principal value [48] of the singular integral with the kernel d:

$$d(\boldsymbol{x}) = \frac{2x_3^2 - x_1^2 - x_2^2}{4\pi|\boldsymbol{x}|^5}.$$

In the frequency domain, (1.3) reads

$$\mathcal{F}(b_l)(\boldsymbol{\xi}) = \mathcal{D}(\boldsymbol{\xi})\mathcal{F}(\chi)(\boldsymbol{\xi}) = \left(\frac{1}{3} - \frac{\xi_3^2}{|\boldsymbol{\xi}|^2}\right)\mathcal{F}(\chi)(\boldsymbol{\xi}), \tag{1.4}$$

where $\mathcal{D} = \mathcal{F}(d)$ is the Fourier transform of d and $\mathcal{D}(\mathbf{0}) = 0$ by the definition of pv [13, 24]. From (1.4), it is easy to see that recovering the susceptibility distribution χ is ill-posed as $\mathcal{D} = 0$ on the critical manifold $\Gamma_0 = \left\{\boldsymbol{\xi} \in \mathbb{R}^3 : \xi_1^2 + \xi_2^2 - 2\xi_3^2 = 0\right\}$. This ill-posedness leads to the streaking artifacts unless the data b_l satisfies a proper compatibility condition [9].

1.1. Existing QSM reconstruction methods. In the literature, various QSM reconstruction methods have been explored to deal with the ill-posed nature of the inverse problem (1.4). Early attempts mainly focus on the direct methods based on the modification of (1.4) near Γ_0 [27]. One benchmark method, called the truncated K-space division (TKD) [47], finds the approximate solution to (1.4) via

$$\chi_\hbar = \mathcal{F}^{-1}(\mathcal{X}_\hbar), \quad \text{where} \quad \mathcal{X}_\hbar(\boldsymbol{\xi}) = \frac{\operatorname{sign}(\mathcal{D}(\boldsymbol{\xi}))}{\max\{|\mathcal{D}(\boldsymbol{\xi})|, \hbar\}}\mathcal{F}(b_l)(\boldsymbol{\xi}), \tag{1.5}$$

with a threshold level $\hbar > 0$. Another method recovers χ by solving the following Tikhonov regularization [29]:

$$\min_{\chi} \ \frac{1}{2}\left\|A\chi - b_l\right\|_2^2 + \varepsilon\left\|\chi\right\|_2^2, \tag{1.6}$$

where $\varepsilon > 0$ and A denotes the forward operator that is obtained by discretizing the kernel $\mathcal{D}$. Recently, some other direct methods have been proposed, e.g., iterative susceptibility weighted imaging and susceptibility mapping [49], analytic continuation [39], and so on. Even though these direct methods are simple to implement, they can introduce additional artifacts due to the modification of $1/\mathcal{D}$ near Γ_0 in the frequency domain [9, 27, 40].

In recent years, regularization-based methods have been proposed and have shown superior performance over the direct method [27, 51]. Mathematically, it is formulated as solving the minimization problem

$$\min_{\chi} \ F(b_l|\chi) + R(\chi), \tag{1.7}$$

where $F(b_l|\chi)$ denotes the data fidelity term and $R(\chi)$ is the regularization term which mostly promotes the sparse approximation of χ under some linear transformation such as total variation and wavelet frames. According to the choices of $F(b_l|\chi)$, the regularization-based methods can be classified under *integral approaches* and *differential approaches* [27]. The most widely used integral approaches are based on the convolution relation (1.3). For example, $F(b_l|\chi) = \frac{1}{2}\left\|A\chi - b_l\right\|_2^2$ when the data is corrupted by a white Gaussian noise. Even though the integral approach is capable of suppressing streaking artifacts, it is empirically reported in [27] that the reconstructed image can contain the shadow artifacts in the region of piecewise constant susceptibility. The differential approaches are based on the partial differential equation (PDE)

$$-\Delta b_l(\boldsymbol{x}) = P(D)\chi(\boldsymbol{x}) = \left(-\frac{1}{3}\Delta + \frac{\partial^2}{\partial x_3^2}\right)\chi(\boldsymbol{x}), \qquad \boldsymbol{x} \in \Omega, \tag{1.8}$$

which is derived from Maxwell's equation [23, 45]. In this case, one typical fidelity term is $F(b_l|\chi) = \frac{1}{2}\|P(D)\chi + \Delta b_l\|_2^2$ by considering $-\Delta b_l$ as a measurement. Compared with the integral approach, the differential approach is able to restore the susceptibility image with fewer shadow artifacts. However, the noise in the data can be amplified by $-\Delta$, which leads to the streaking artifacts [52]. In [27], the differential approach is implemented by incorporating the spherical mean value (SMV) filter S_r with a radius $r > 0$ [30] into the integral approach:

$$\min_{\chi} \frac{1}{2}\|S_r(A\chi - b_l)\|_2^2 + R(\chi). \tag{1.9}$$

Since the implementation of S_r causes the erosion of Ω according to the choice of r, the loss of anatomical information near $\partial\Omega$ is inevitable at the cost of the shadow artifact removal [27].

1.2. Motivations and contributions of our approach. Even though (1.3) and (1.8) are known to be equivalent [9, 27, 40], it is observed that the local field b_l defined as (1.3) is a particular solution of the PDE (1.8). Whenever the data acquisition is based on the PDE (1.8), the measured local field data will be written as the superposition of b_l in (1.3) and the ambiguity of $-\Delta$, which will be referred to as the *harmonic incompatibility*. Therefore, there is a need to identify/remove the harmonic incompatibility from the measured local field data for better reconstruction results as it is smooth and analytic and satisfies the mean value property in an open set [19], which are different from the noise properties.

It is noted that the background field removal aims at obtaining the local field b_l via solving a Poisson equation with certain boundary condition as the background field is harmonic in Ω [30, 43, 52, 57]. In this case, the measured local field b_l is represented by the Green's function associated with the boundary condition [9]. Thus, it is inevitable that b_l contains the incompatibility associated with the imposed boundary condition. In this paper, we investigate the incompatibility of the local field data in QSM and establish that this incompatibility consists of two harmonic functions inside and outside Ω, respectively, and its (distributional) Laplacian defines a surface measure on $\partial\Omega$ (see Theorem 2.2 for details and Figures 2 to 5 for illustrations). Therefore, we can establish a new forward model in QSM by taking this harmonic incompatibility into account.

Based on this discovery, we impose a constraint on the harmonic incompatibility term in the susceptibility reconstruction model. Since our theoretical results suggest that the incompatibility is harmonic except on $\partial\Omega$, one straightforward approach is to penalize its (discrete) Laplacian on points $\boldsymbol{x} \notin \partial\Omega$. However, it is in general difficult to explicitly model this harmonic incompatibility and/or to directly impose its property onto the susceptibility reconstruction model due to the complicated geometries of human brains and the limited spatial resolution in real MRI data. Instead, we impose the sparse regularization of the incompatibility, as the support of its Laplacian is small compared to the size of the image. Combining it with traditional regularization on the susceptibility image, we propose a novel regularization-based QSM model by imposing additional constraints on the incompatibility term. Within the new model, we can suppress the incompatibility other than the noise, achieving the whole brain imaging with fewer artifacts together with the regularization of the susceptibility image. Experiments on both brain phantom and in vivo MR data consistently show the advantages of the proposed harmonic incompatibility removal (HIRE) model, which achieves state-of-the-art performance. In addition, our experiments suggest that tight frame

regularization of the susceptibility image can avoid the constant offset [27] and lead to efficient computation.

1.3. Organization of paper. In section 2, we introduce our HIRE model for whole brain susceptibility imaging. More precisely, we first briefly review the biophysics forward model of QSM in subsection 2.1 and characterize the harmonic incompatibility in the local field data in subsection 2.2. Based on the characterization, we introduce the proposed HIRE model in subsection 2.3, followed by an alternating minimization algorithm in subsection 2.4. In section 3, we present experimental results for both brain phantom and in vivo MR data, and concluding remarks are given in section 4.

2. Harmonic incompatibility removal (HIRE) model for whole brain imaging.

2.1. Preliminaries on biophysics of QSM. In an MRI scanner with the main static magnetic field $\mathbf{B}_0 = (0, 0, B_0)$, where B_0 is a positive constant, objects gain a magnetization $\mathbf{M}(\boldsymbol{x})$. This magnetization generates a macroscopic field $\mathbf{B}(\boldsymbol{x})$ satisfying the following magnetostatic Maxwell equation [23, 45]:

$$\begin{aligned} \nabla \cdot \mathbf{B} &= 0, \\ \nabla \times \mathbf{B} &= \mu_0 \nabla \times \mathbf{M}, \end{aligned} \tag{2.1}$$

where $\mu_0 = 8.854 \times 10^{-12}$F/m is the vacuum permittivity. Since the MRI signal is generated by the microscopic field $\mathbf{B}_\ell(\boldsymbol{x})$ experienced by the spins of water protons [27], to relate $\mathbf{B}(\boldsymbol{x})$ and $\mathbf{B}_\ell(\boldsymbol{x})$ we use the following Lorenz sphere correction model [23]:

$$\mathbf{B}_\ell(\boldsymbol{x}) = \mathbf{B}(\boldsymbol{x}) - \frac{2}{3}\mu_0 \mathbf{M}(\boldsymbol{x}). \tag{2.2}$$

Note that since $\mathbf{M}(\boldsymbol{x})$ is generated by the $\mathbf{B}_0$ field, we have $\mathbf{M}(\boldsymbol{x}) = (0, 0, M(\boldsymbol{x}))$. Moreover, since we consider the linear magnetic materials with $|\chi| \ll 1$, χ can be approximated as

$$\chi(\boldsymbol{x}) \approx \frac{\mu_0}{B_0} M(\boldsymbol{x}). \tag{2.3}$$

Finally, we introduce the total field $b(\boldsymbol{x})$ as

$$b(\boldsymbol{x}) = \frac{B_{\ell 3}(\boldsymbol{x}) - B_0}{B_0}, \tag{2.4}$$

where $B_{\ell 3}(\boldsymbol{x})$ denotes the third component of $\mathbf{B}_\ell(\boldsymbol{x})$.

Combining (2.1)–(2.4) and taking only the third component into account, we obtain the following relation between χ and b in the frequency domain:

$$|\boldsymbol{\xi}|^2 \mathcal{F}(b)(\boldsymbol{\xi}) = \left(\frac{1}{3}|\boldsymbol{\xi}|^2 - \xi_3^2\right) \mathcal{F}(\chi)(\boldsymbol{\xi}), \tag{2.5}$$

which gives

$$-\Delta b = P(D)\chi := \left(-\frac{1}{3}\Delta + \frac{\partial^2}{\partial x_3^2}\right) \chi. \tag{2.6}$$

Then for a given susceptibility distribution χ (in $\mathbb{R}^3$), the general solution b, which is bounded everywhere in $\mathbb{R}^3$, is expressed as

$$b(\boldsymbol{x}) = \int_{\mathbb{R}^3} \Phi(\boldsymbol{x}-\boldsymbol{y}) \left(-\frac{1}{3}\Delta_{\boldsymbol{y}} + \frac{\partial^2}{\partial y_3^2}\right) \chi(\boldsymbol{y}) \mathrm{d}\boldsymbol{y} + b_0, \tag{2.7}$$

where b_0 is some constant, and $\Phi(\boldsymbol{x}) = 1/(4\pi|\boldsymbol{x}|)$.

In MRI, the phase of a complex GRE MR signal is linear with respect to the total field b in (2.7) [52], and the constant b_0 is determined by the coil sensitivity of an MR scanner as the coil sensitivity–dependent phase offset is in general assumed to be a constant [24, 44]. However, since we can remove it during the phase estimation from the multiecho GRE signal [12], we assume that $b_0 = 0$ and

$$b(\boldsymbol{x}) = \int_{\mathbb{R}^3} \Phi(\boldsymbol{x}-\boldsymbol{y}) \left(-\frac{1}{3}\Delta_{\boldsymbol{y}} + \frac{\partial^2}{\partial y_3^2}\right) \chi(\boldsymbol{y}) \mathrm{d}\boldsymbol{y} \tag{2.8}$$

in the rest of this paper. Note that b defined as above is induced by the susceptibility distribution *in the entire space,* which is different from b_l in (1.3).

Remark 2.1. Since [9, Proposition A.1] has discussed the equivalence between (2.8) and the representation

$$b(\boldsymbol{x}) = \mathrm{pv} \int_{\mathbb{R}^3} d(\boldsymbol{x}-\boldsymbol{y}) \chi(\boldsymbol{y}) \mathrm{d}\boldsymbol{y} \tag{2.9}$$

in the literature, we shall use (2.8) in the rest of this paper. Note that (2.8) avoids the singularity of the kernel $d(\boldsymbol{x}-\boldsymbol{y})$ in (2.9) as $\Phi(\boldsymbol{x}-\boldsymbol{y})$ is locally integrable near $\boldsymbol{x} = \boldsymbol{y}$.

2.2. Characterization of harmonic incompatibility in local field data. In QSM, the total field $b(\boldsymbol{x})$ is obtained from the phase data of a complex GRE MR signal [44, 52]. In fact, if the information of b is available over the entire space, then we can directly solve the inverse problem from the knowledge of b without the background field removal step. However, since the GRE signal is not available outside Ω, the information of b is available only inside Ω. Moreover, even if χ is compactly supported, the support of b may not necessarily coincide with that of χ, which inevitably leads to the information loss outside Ω [44, 52].

Since the total field b depends on the susceptibility distribution *throughout the entire space* [44], it consists of the background field induced from the susceptibility outside Ω, which is of no interest, and the local field b_l by the susceptibility in Ω which we aim to visualize. Since the substantial susceptibility sources are usually located outside Ω, which makes the background field dominant in b compared to the local field b_l, we need to remove the background field from the (incomplete) total field prior to the dipole inversion [44, 52].

In the literature, given that the background field is harmonic in Ω [52, 57], the background field removal methods take the form of the following Poisson equation in [57]:

$$\begin{cases} -\Delta b_l = -\Delta b & \text{in } \Omega, \\ b_l = 0 & \text{on } \partial\Omega. \end{cases} \tag{2.10}$$

Under this setting, we present Theorem 2.2, which characterizes the relation between (2.10) and the PDE (2.6), and the measured local field obtained by solving (2.10) contains an incompatibility which consists of two harmonic functions both inside and outside Ω due to the imposed boundary condition.

Theorem 2.2. *Let $\Omega \subseteq \mathbb{R}^3$ be an open and bounded set with C^1 boundary $\partial\Omega$. Let b satisfy (2.8) for a given χ compactly supported in $\mathbb{R}^3$, and let $b_l : \overline{\Omega} \to \mathbb{R}$ be obtained from (2.10). If we extend b_l into $\mathbb{R}^3$ by assigning $b_l(\boldsymbol{x}) = 0$ for $\boldsymbol{x} \notin \Omega$, then we have the following:*

1. *There exists $v(x)$ such that*

$$b_l(\boldsymbol{x}) = \int_\Omega \Phi(\boldsymbol{x}-\boldsymbol{y}) \left(-\frac{1}{3}\Delta_{\boldsymbol{y}} + \frac{\partial^2}{\partial y_3^2}\right) \chi(\boldsymbol{y}) \mathrm{d}\boldsymbol{y} + v(\boldsymbol{x}) \tag{2.11}$$

for $\boldsymbol{x} \in \mathbb{R}^3$, and $v(\boldsymbol{x})$ satisfies

$$\int_{\mathbb{R}^3} v(\boldsymbol{x}) \left(-\Delta\varphi\right)(\boldsymbol{x}) \mathrm{d}\boldsymbol{x} = \int_{\partial\Omega} \left[\frac{\partial v_{\mathrm{i}}}{\partial \boldsymbol{n}}(\boldsymbol{x}) - \frac{\partial v_{\mathrm{e}}}{\partial \boldsymbol{n}}(\boldsymbol{x})\right] \varphi(\boldsymbol{x}) \mathrm{d}\boldsymbol{\sigma}(\boldsymbol{x}) \tag{2.12}$$

for $\varphi \in C_0^\infty(\mathbb{R}^3)$, where v_{i} and v_{e} denote the restriction of v in $\overline{\Omega}$ and $\mathbb{R}^3 \setminus \Omega$, respectively, and $\boldsymbol{n}$ denotes the outward unit normal vector of $\partial\Omega$.

2. *Moreover, we have*

$$\frac{\partial v_{\mathrm{i}}}{\partial \boldsymbol{n}} - \frac{\partial v_{\mathrm{e}}}{\partial \boldsymbol{n}} \neq 0 \quad \text{almost everywhere on } \partial\Omega \tag{2.13}$$

whenever $P(D)\chi \neq 0$ in Ω. Hence, $-\Delta v = 0$ in $\mathbb{R}^3 \setminus \partial\Omega$, and $-\Delta v \neq 0$ on $\partial\Omega$ in this case.

Proof. Since $-\Delta b = P(D)\chi$, the governing equation in (2.10) becomes

$$\begin{cases} -\Delta b_l = P(D)\chi & \text{in } \Omega, \\ b_l = 0 & \text{on } \partial\Omega. \end{cases}$$

Let $G(\boldsymbol{x}, \boldsymbol{y})$ denote the Green's function in Ω:

$$G(\boldsymbol{x}, \boldsymbol{y}) = \Phi(\boldsymbol{y}-\boldsymbol{x}) - H(\boldsymbol{x}, \boldsymbol{y}),$$

where for each $\boldsymbol{x} \in \Omega$ the corrector function $H(\boldsymbol{x}, \boldsymbol{y})$ satisfies

$$\begin{cases} -\Delta_{\boldsymbol{y}} H(\boldsymbol{x}, \boldsymbol{y}) = 0 & \text{if } \boldsymbol{y} \in \Omega, \\ H(\boldsymbol{x}, \boldsymbol{y}) = \Phi(\boldsymbol{y}-\boldsymbol{x}) & \text{if } \boldsymbol{y} \in \partial\Omega. \end{cases}$$

Note that since $G(\boldsymbol{x}, \boldsymbol{y}) = G(\boldsymbol{y}, \boldsymbol{x})$ for $\boldsymbol{x}, \boldsymbol{y} \in \Omega$ and $\Phi(\boldsymbol{y}-\boldsymbol{x}) = \Phi(\boldsymbol{x}-\boldsymbol{y})$, we have $H(\boldsymbol{x}, \boldsymbol{y}) = H(\boldsymbol{y}, \boldsymbol{x})$ for $\boldsymbol{x}, \boldsymbol{y} \in \Omega$. Consequently, we have

$$-\Delta_{\boldsymbol{x}} H(\boldsymbol{x}, \boldsymbol{y}) = -\Delta_{\boldsymbol{x}} H(\boldsymbol{y}, \boldsymbol{x}) = 0, \qquad \boldsymbol{x} \in \Omega. \tag{2.14}$$

Then the solution to (2.10) is represented by

$$b_l(\boldsymbol{x}) = \int_\Omega G(\boldsymbol{x}, \boldsymbol{y}) P(D_{\boldsymbol{y}}) \chi(\boldsymbol{y}) \mathrm{d}\boldsymbol{y} = \int_\Omega \Phi(\boldsymbol{x}-\boldsymbol{y}) P(D_{\boldsymbol{y}}) \chi(\boldsymbol{y}) \mathrm{d}\boldsymbol{y} + \mathcal{H}(\boldsymbol{x}),$$

where we used the fact that $\Phi(\boldsymbol{y}-\boldsymbol{x}) = \Phi(\boldsymbol{x}-\boldsymbol{y})$, and $\mathcal{H}(\boldsymbol{x})$ is defined as

$$\mathcal{H}(\boldsymbol{x}) = -\int_\Omega H(\boldsymbol{x},\boldsymbol{y})P(D_{\boldsymbol{y}})\chi(\boldsymbol{y})\mathrm{d}\boldsymbol{y}$$

for $\boldsymbol{x}\in\Omega$. Then we can see that $\mathcal{H}(\boldsymbol{x})$ satisfies

$$\begin{cases} -\Delta\mathcal{H} = 0 & \text{in } \Omega, \\ \mathcal{H} = -\widetilde{b}_l & \text{on } \partial\Omega, \end{cases} \tag{2.15}$$

where the first equation of (2.15) comes from (2.14). Here, $\widetilde{b}_l$ is induced by the information of χ only in Ω:

$$\widetilde{b}_l(\boldsymbol{x}) = \int_\Omega \Phi(\boldsymbol{x}-\boldsymbol{y})P(D_{\boldsymbol{y}})\chi(\boldsymbol{y})\mathrm{d}\boldsymbol{y} = \int_{\mathbb{R}^3} \Phi(\boldsymbol{x}-\boldsymbol{y})1_\Omega(\boldsymbol{y})P(D_{\boldsymbol{y}})\chi(\boldsymbol{y})\mathrm{d}\boldsymbol{y}, \tag{2.16}$$

with 1_Ω being the characteristic function of Ω.

Based on the fact that $b_l(\boldsymbol{x}) = 0$ for $\boldsymbol{x}\in\mathbb{R}^3\setminus\overline{\Omega}$, we define

$$v(\boldsymbol{x}) = \begin{cases} v_{\mathrm{i}}(\boldsymbol{x}) = \mathcal{H}(\boldsymbol{x}) & \text{if } \boldsymbol{x}\in\Omega, \\ v_{\mathrm{e}}(\boldsymbol{x}) = -\widetilde{b}_l(\boldsymbol{x}) & \text{if } \boldsymbol{x}\notin\Omega. \end{cases}$$

Hence, we obtain (2.11), and we can further see that v_{i} and v_{e} satisfy

$$-\Delta v_{\mathrm{i}} = 0 \quad \text{in } \Omega, \tag{2.17}$$

$$-\Delta v_{\mathrm{e}} = 0 \quad \text{in } \mathbb{R}^3\setminus\overline{\Omega}, \tag{2.18}$$

$$v_{\mathrm{i}} = v_{\mathrm{e}} = -\widetilde{b}_l \quad \text{on } \partial\Omega, \tag{2.19}$$

respectively, where (2.18) comes from (2.16); $-\Delta\widetilde{b}_l = 1_\Omega P(D)\chi$, i.e., $-\Delta\widetilde{b}_l = P(D)\chi$ in Ω, and $-\Delta\widetilde{b}_l = 0$ in $\mathbb{R}^3\setminus\overline{\Omega}$.

To prove (2.12), let $\varphi\in C_0^\infty(\mathbb{R}^3)$, and we consider

$$\begin{aligned}\int_{\mathbb{R}^3} v(\boldsymbol{x})\left(-\Delta\varphi\right)(\boldsymbol{x})\mathrm{d}\boldsymbol{x} &= \int_\Omega v_{\mathrm{i}}(\boldsymbol{x})\left(-\Delta\varphi\right)(\boldsymbol{x})\mathrm{d}\boldsymbol{x} + \int_{\mathbb{R}^3\setminus\overline{\Omega}} v_{\mathrm{e}}(\boldsymbol{x})\left(-\Delta\varphi\right)(\boldsymbol{x})\mathrm{d}\boldsymbol{x} \\ &= I_1 + I_2.\end{aligned}$$

Using (2.17) and (2.19) and the Green's identity (see, e.g., [19]), we have

$$\begin{aligned} I_1 &= \int_\Omega \left[\varphi(\boldsymbol{x})\left(\Delta v_{\mathrm{i}}\right)(\boldsymbol{x}) - v_{\mathrm{i}}(\boldsymbol{x})\left(\Delta\varphi\right)(\boldsymbol{x})\right]\mathrm{d}\boldsymbol{x} \\ &= \int_{\partial\Omega}\left[\varphi(\boldsymbol{x})\frac{\partial v_{\mathrm{i}}}{\partial\boldsymbol{n}}(\boldsymbol{x}) - v_{\mathrm{i}}(\boldsymbol{x})\frac{\partial\varphi}{\partial\boldsymbol{n}}(\boldsymbol{x})\right]\mathrm{d}\boldsymbol{\sigma}(\boldsymbol{x}) = \int_{\partial\Omega}\left[\varphi(\boldsymbol{x})\frac{\partial v_{\mathrm{i}}}{\partial\boldsymbol{n}}(\boldsymbol{x}) + \widetilde{b}_l(\boldsymbol{x})\frac{\partial\varphi}{\partial\boldsymbol{n}}(\boldsymbol{x})\right]\mathrm{d}\boldsymbol{\sigma}(\boldsymbol{x}). \end{aligned}$$

Similarly using (2.18) and (2.19), we also have

$$\begin{aligned} I_2 &= \int_{\mathbb{R}^3\setminus\overline{\Omega}}\left[\varphi(\boldsymbol{x})\left(\Delta v_{\mathrm{e}}\right)(\boldsymbol{x}) - v_{\mathrm{e}}(\boldsymbol{x})\left(\Delta\varphi\right)(\boldsymbol{x})\right]\mathrm{d}\boldsymbol{x} \\ &= \int_{\partial\Omega}\left[-\varphi(\boldsymbol{x})\frac{\partial v_{\mathrm{e}}}{\partial\boldsymbol{n}}(\boldsymbol{x}) + v_{\mathrm{e}}(\boldsymbol{x})\frac{\partial\varphi}{\partial\boldsymbol{n}}(\boldsymbol{x})\right]\mathrm{d}\boldsymbol{\sigma}(\boldsymbol{x}) = -\int_{\partial\Omega}\left[\varphi(\boldsymbol{x})\frac{\partial v_{\mathrm{e}}}{\partial\boldsymbol{n}}(\boldsymbol{x}) + \widetilde{b}_l(\boldsymbol{x})\frac{\partial\varphi}{\partial\boldsymbol{n}}(\boldsymbol{x})\right]\mathrm{d}\boldsymbol{\sigma}(\boldsymbol{x}), \end{aligned}$$

where the second equality comes from the fact that we need to compute the inward normal derivatives on $\partial\Omega$. Hence, combining these two equalities, we obtain (2.12).

To prove statement 2, we assume on the contrary that there exists $\boldsymbol{x} \in \partial\Omega$ such that

$$\frac{\partial v_{\mathrm{i}}}{\partial \boldsymbol{n}} = \frac{\partial v_{\mathrm{e}}}{\partial \boldsymbol{n}}$$

for some open and connected set $U \subseteq \partial\Omega$ such that $\boldsymbol{x} \in U$ and $\boldsymbol{\sigma}(U) > 0$. Choose $r > 0$ such that $B(\boldsymbol{x}, r) \cap \partial\Omega$ is contained in U, where $B(\boldsymbol{x}, r)$ denotes an open ball centered at $\boldsymbol{x}$ with radius r. Then, since $-\Delta v = 0$ in $B(\boldsymbol{x}, r)$ and $v = v_{\mathrm{e}} = -\widetilde{b}_l$ in $B(\boldsymbol{x}, r) \cap \left(\mathbb{R}^3 \setminus \overline{\Omega}\right)$, it follows that $v = -\widetilde{b}_l$ in $B(\boldsymbol{x}, r)$ by the analyticity of v in $B(\boldsymbol{x}, r)$. Since this means that $v = v_{\mathrm{i}} = -\widetilde{b}_l$ in $B(\boldsymbol{x}, r) \cap \Omega$, together with the fact that v_{i} is harmonic in Ω, we have $v_{\mathrm{i}} = -\widetilde{b}_l$ in Ω by the analyticity of v_{i} in Ω. Since $v = -\widetilde{b}_l$ on $\partial\Omega$, we have $v = -\widetilde{b}_l$ in $\mathbb{R}^3$. Hence, $-\Delta\widetilde{b}_l = 0$ in $\mathbb{R}^3$, and thus $P(D)\chi = 0$ in Ω, which is a contradiction. ∎

Remark 2.3. From the proof of Theorem 2.2, the incompatibility v in (2.11) is from the boundary condition of (2.10), which is not related to the regularity of χ. More precisely, v_{i} inside Ω is generated by the information of the unknown true local field $\widetilde{b}_l$ on $\partial\Omega$ so that the boundary condition of (2.10) is matched. In addition, it is obvious that v_{e} outside Ω is due to the information loss outside Ω.

Remark 2.4. Notice that $P(D)$ is a "wave-type" differential operator (by considering x_3 as the time variable). Indeed, the proof of (2.13) tells us that if $P(D)\chi = 0$ in Ω, such χ has a wave-type structure in Ω regardless of its regularity, whereas the susceptibility of the human brain does not have such a wave-type structure [9]. Hence in QSM, it follows that $-\Delta v$ defined as (2.12) is a nonvanishing surface measure on $\partial\Omega$, i.e., $-\Delta v = 0$ in $\mathbb{R}^3 \setminus \partial\Omega$, but $-\Delta v \neq 0$ on $\partial\Omega$.

We present Figures 2 to 5 to illustrate Theorem 2.2 by using the Shepp–Logan phantom (Figures 2 and 3) and the brain phantom (Figures 4 and 5). Using the limited total field b in Figures 2(d), 3(d), 4(d), and 5(d), which are derived from (2.8) by placing strong susceptibilities outside Ω, we solve (2.10) using the multigrid-based finite difference method [57] to obtain the measured local field b_l in Figures 2(f), 3(f), 4(f), and 5(f), which are used for the susceptibility reconstruction. We also display the true local field $\widetilde{b}_l$ obtained from (2.16) in Figures 2(e), 3(e), 4(e), and 5(e) for comparison with the measured b_l. Finally, $v = b_l - \widetilde{b}_l$ and $|-\Delta v|$ are displayed in Figures 2(g), 3(g), 4(g), and 5(g) and Figures 2(h), 3(h), 4(h), and 5(h), respectively, for better illustration. Compared to the Shepp–Logan phantom, the brain phantom shows the artifacts as shown in Figure 4(h). There are two possible reasons for the artifacts. First, since the boundary of the human brain is more complicated than the Shepp–Logan phantom, the erroneous boundary values may have affected the background field removal in the case of the brain phantom, as pointed out in [57]. Second, unlike the Shepp–Logan phantom with isotropic spatial resolution ($1 \times 1 \times 1\mathrm{mm}^3$), the brain phantom has an anisotropic spatial resolution of $0.9375 \times 0.9375 \times 1.5\mathrm{mm}^3$. As pointed out in [20], the multigrid method has the limitation that errors in certain directions (the x_3 direction in our case) are not smoothed by standard relaxation, and as a consequence it is inappropriate to coarsen in these directions, which may lead to artifacts in Figure 4(h) along the x_3 direction. Since the real spatial resolution of phase data is not necessarily isotropic, an efficient and

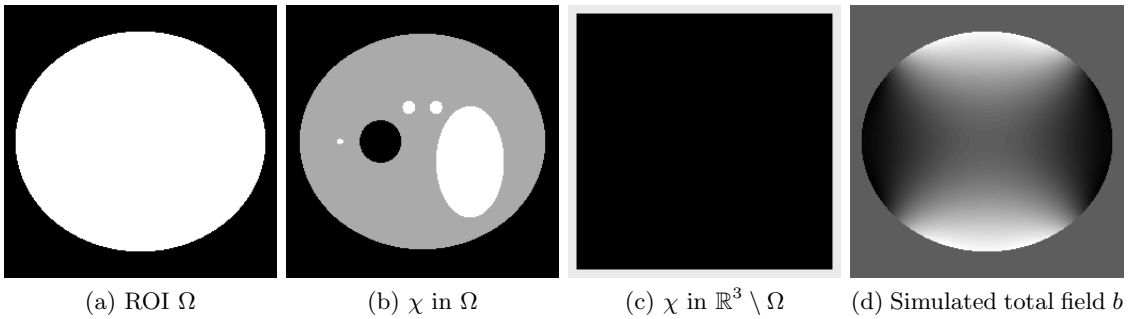

(a) ROI Ω (b) χ in Ω (c) χ in $\mathbb{R}^3 \setminus \Omega$ (d) Simulated total field b

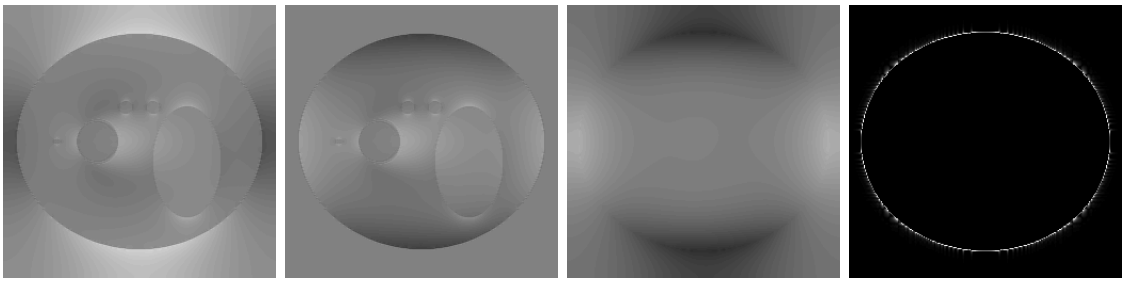

(e) True local field $\widetilde{b}_l$ (f) Measured local field b_l (g) $v = b_l - \widetilde{b}_l$ (h) $|-\Delta v|$

Figure 2. *Sagittal slice images of* $256 \times 256 \times 256$ *Shepp–Logan phantom with* $1 \times 1 \times 1\text{mm}^3$. χ *in* $\mathbb{R}^3 \setminus \Omega$ *is displayed in the window level* $[0, 550]$, $\widetilde{b}_l$, b_l, *and* v *in the window level* $[-0.025, 0.025]$, *and* $|-\Delta v|$ *in the window level* $[0, 0.001]$.

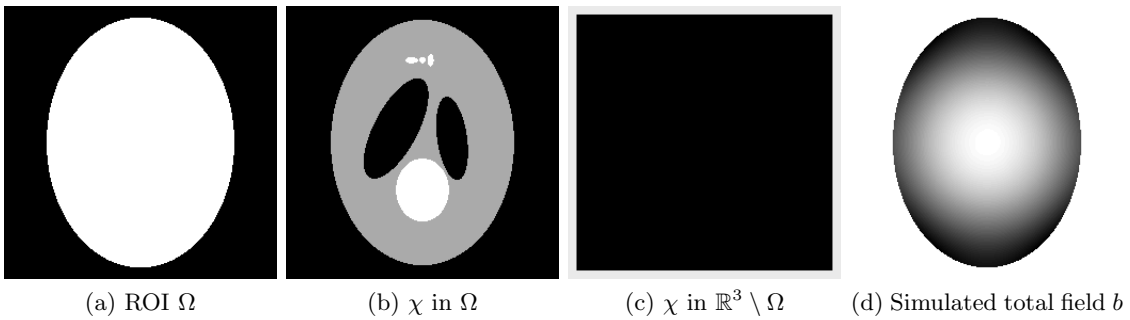

(a) ROI Ω (b) χ in Ω (c) χ in $\mathbb{R}^3 \setminus \Omega$ (d) Simulated total field b

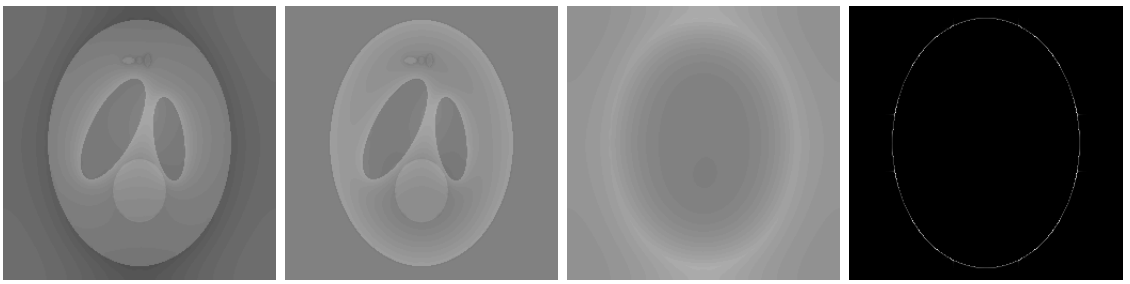

(e) True local field $\widetilde{b}_l$ (f) Measured local field b_l (g) $v = b_l - \widetilde{b}_l$ (h) $|-\Delta v|$

Figure 3. *Axial slice images of Figure 2. The images of* χ *in* $\mathbb{R}^3 \setminus \Omega$, $\widetilde{b}_l$, b_l, v, *and* $|-\Delta v|$ *are displayed in the same window level as in Figure 2.*

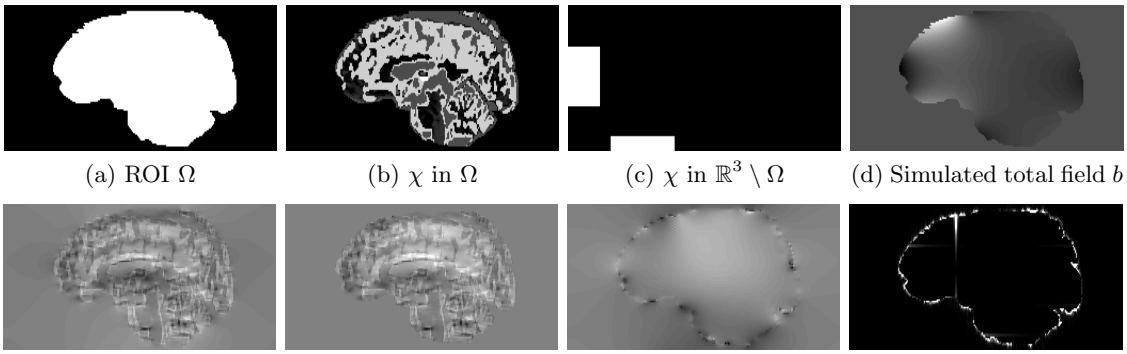

(a) ROI Ω (b) χ in Ω (c) χ in $\mathbb{R}^3 \setminus \Omega$ (d) Simulated total field b

(e) True local field $\widetilde{b}_l$ (f) Measured local field b_l (g) $v = b_l - \widetilde{b}_l$ (h) $|-\Delta v|$

Figure 4. *Sagittal slice images of* $256 \times 256 \times 98$ *brain phantom images with* $0.9375 \times 0.9375 \times 1.5\text{mm}^3$. *Image of* χ *in* $\mathbb{R}^3 \setminus \Omega$ *is displayed in the window level* $[0, 500]$, $\widetilde{b}_l$ *and* b_l *in the window level* $[-0.05, 0.05]$, v *in the window level* $[-0.025, 0.025]$, *and* $|-\Delta v|$ *in the window level* $[0, 0.01]$, *respectively.*

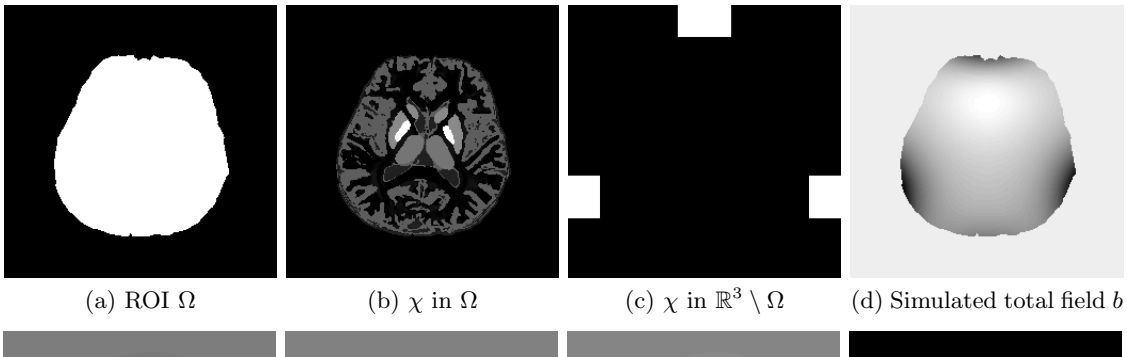

(a) ROI Ω (b) χ in Ω (c) χ in $\mathbb{R}^3 \setminus \Omega$ (d) Simulated total field b

(e) True local field $\widetilde{b}_l$ (f) Measured local field b_l (g) $v = b_l - \widetilde{b}_l$ (h) $|-\Delta v|$

Figure 5. *Axial slice images of Figure 4. The images of* χ *in* $\mathbb{R}^3 \setminus \Omega$, $\widetilde{b}_l$, b_l, v, *and* $|-\Delta v|$ *are displayed in the same window level as in Figure 4.*

effective numerical solver of (2.10) needs to be investigated in the future, which is beyond the scope of this paper at this point.

2.3. Proposed HIRE susceptibility reconstruction model. We begin by introducing some notation. Let $\mathbb{O} = \{0, \dots, N_1 - 1\} \times \{0, \dots, N_2 - 1\} \times \{0, \dots, N_3 - 1\}$ denote the set of indices of $N_1 \times N_2 \times N_3$ grids, and let $\Omega \subseteq \mathbb{O}$ denote the set of indices corresponding to the ROI. Denote $\partial\Omega$ to be the indices of the boundary of ROI Ω. Finally, the space of real-valued

functions defined on $\mathbb{O}$ is denoted as $\mathcal{I}_3 \simeq \mathbb{R}^{N_1 \times N_2 \times N_3}$.

Let $b_l \in \mathcal{I}_3$ be the (noisy) measured local field data obtained from (2.10), which satisfies $b_l = 0$ in $\mathbb{O} \setminus \Omega$. From the viewpoint of Theorem 2.2, we can model it as

$$b_l = A\chi + v + \eta,$$

where $A = \mathcal{F}^{-1}\mathcal{D}\mathcal{F}$ denotes the discretization of the forward operator in (2.11). Here, $\chi \in \mathcal{I}_3$ is the unknown true susceptibility image supported in Ω, $v \in \mathcal{I}_3$ is the incompatibility arising from solving (2.10), and η is the additive noise.

We observe that in the discrete setting, (2.12) in Theorem 2.2 can be understood as

$$\mathcal{L}v = 0 \quad \text{in} \quad \mathbb{O} \setminus \partial\Omega \quad \text{and} \quad \mathcal{L}v \neq 0 \quad \text{on} \quad \partial\Omega \tag{2.20}$$

with the discrete Laplacian $\mathcal{L}$, as $\mathcal{L}v$ is supported on $\partial\Omega$. However, it is in general difficult to directly impose (2.20) onto the susceptibility reconstruction model (e.g., penalizing $\|(\mathcal{L}v)_{\mathbb{O}\setminus\partial\Omega}\|_2^2$) for the following reasons: (1) the estimation of Ω always contains error due to the complicated geometry of the human brain; (2) the real MRI data may not exactly satisfy (2.20) due to its spatial resolution [23]; (3) the discretization can introduce the error on the boundary of Ω. However, it is a fact that the support of $\mathcal{L}v$ is small compared to $|\mathbb{O}| = N_1N_2N_3$; i.e., $\mathcal{L}v$ is sparse. Consequently, we penalize the $\|\mathcal{L}v\|_1$ for the incompatibility term v. Although the $\|\mathcal{L}v\|_1$ does not necessarily satisfy the harmonic constraints on $\mathbb{O}\setminus\partial\Omega$, it is a good relaxation approach when considering the error source of the forward model in QSM. In addition, motivated by the successful results on the wavelet frame–based image restoration (e.g., [3, 4]), we assume the sparse approximation of χ under a given wavelet transformation W and propose our HIRE model as follows:

$$\min_{\chi, v \in \mathcal{I}_3} \frac{1}{2}\|A\chi + v - b_l\|_\Sigma^2 + \lambda\|\mathcal{L}v\|_1 + \|\gamma \cdot W\chi\|_{1,2}, \tag{2.21}$$

where $\|\cdot\|_\Sigma^2 = \langle \Sigma\cdot, \cdot\rangle$ with the SNR weight Σ which is estimated from the MRI [32, 38]. Here, $\|\gamma \cdot W\chi\|_{1,2}$ is the isotropic ℓ_1 norm of the wavelet frame coefficients [4] defined as

$$\|\gamma \cdot W\chi\|_{1,2} := \sum_{\boldsymbol{k}\in\mathbb{O}} \sum_{l=0}^{L-1} \gamma_l[\boldsymbol{k}] \left(\sum_{\boldsymbol{\alpha}\in\mathbb{B}} |(W_{l,\boldsymbol{\alpha}}\chi)[\boldsymbol{k}]|^2 \right)^{1/2}. \tag{2.22}$$

(See Appendix A for the brief introduction on the wavelet frames.)

There are many variational regularizations for the susceptibility image, including total variation (TV) [42], total generalized variation (TGV) [2, 55], and weighted TV for morphological consistency [26]. However, since $\mathcal{D}(\mathbf{0}) = 0$, the χ subproblem is a rank deficient system matrix, when using the alternating direction method of multipliers (ADMM) methods [18] to solve the regularization model. As a consequence, we may need additional prior information such as the zero susceptibility value in the cerebrospinal fluid region [36] for stable reconstruction. In contrast, by using tight frame regularization, the system matrix of χ subproblem has a full column rank, which can lead to better computational efficiency than that of existing variational methods.

Remark 2.5. For a better understanding of our HIRE model, we temporarily assume that $\Sigma = I$ and consider

$$\min_{\chi, v \in \mathcal{I}_3} \frac{1}{2} \|A\chi + v - b_l\|_2^2 + \lambda \|\mathcal{L}v\|_1 + \|\gamma \cdot W\chi\|_{1,2}.$$

If $v \equiv 0$, our model reduces to the integral approach model:

$$\min_{\chi \in \mathcal{I}_3} \frac{1}{2} \|A\chi - b_l\|_2^2 + \|\gamma \cdot W\chi\|_{1,2}.$$

In addition, if we fix $v = b_l - A\chi$, our model reduces to the ℓ_1 fidelity version of the following differential approach model:

$$\min_{\chi \in \mathcal{I}_3} \frac{1}{2} \|\mathcal{L}b_l - \mathcal{L}A\chi\|_2^2 + \|\gamma \cdot W\chi\|_{1,2}$$

as $\mathcal{L}A\chi = \mathcal{L}b_l$ discretizes the PDE (2.6) in the sense of [9, Proposition A.1].

From Remark 2.5, we can see that our model considers the incompatibility v and noise separately, thereby providing a more precise forward model for QSM. This is because b_l is obtained from the Poisson equation (2.10), and it inevitably contains the harmonic incompatibility related to the imposed boundary condition, as described in Theorem 2.2. Even though more rigorous theoretical analysis is needed, we can somehow explain the effect of harmonic incompatibility in this manner; since the standard arguments on the harmonic functions (see, e.g., [19]) tell us that v is smooth and satisfies the mean value property except on $\partial\Omega$, it has slow variations on this region. As a consequence, it mostly affects the low frequency components in b_l compared to the noise which mainly affects the high frequency components. Together with the fact that the critical manifold Γ_0 forms a conic manifold in the frequency domain, the harmonic incompatibility v in b_l mainly leads to the loss of $\mathcal{F}(\chi)$ in low frequency components.

As empirically observed in [27], the incompatibility in low frequency components of b_l leads to shadow artifacts in the reconstructed image, while that in high frequency components leads to streaking artifacts. Therefore, a simultaneous consideration of the incompatibilities in both components is crucial for better susceptibility imaging. The integral approach does not take the harmonic incompatibility in b_l into account, which may not be capable of suppressing the incompatibility in low frequency components of b_l, and leads to shadow artifacts in the reconstructed images. The differential approach can be viewed as a preconditioned integral approach since the harmonic incompatibility in b_l has been removed in advance. However, the noise in b_l can be amplified by $\mathcal{L}$ at the cost of harmonic incompatibility removal, and this leads to the streaking artifacts propagating from the noise in the final image [52]. In contrast, the HIRE model takes the form of an integral approach, which explicitly considers the incompatibility v other than the noise by incorporating its sparsity under $\mathcal{L}$. By doing so, we expect that the HIRE model can suppress both the noise (cause of streaking artifacts) and the harmonic incompatibility (cause of shadow artifacts), so that we can achieve the whole brain imaging with fewer artifacts.

We would like to mention that the formulation of the HIRE model is not limited to (2.21). In fact, we can use the nonlinear fidelity term $F(b_l|\chi, v) = \frac{1}{2} \left\| e^{i(A\chi+v)\omega_0 B_0 TE} - e^{ib_l\omega_0 B_0 TE} \right\|_\Sigma^2$

to further compensate for the errors in phase unwrapping, which will be more coincident with the GRE signal model [27, 35]. However, we will not discuss the details of such nonlinear variants as this is beyond the scope of this paper. We will focus on (2.21) throughout this paper.

2.4. Numerical algorithm. In the literature, there are numerous algorithms which can solve the proposed HIRE model (2.21). In this paper, we adopt the split Bregman algorithm given in [38] in the framework of ADMM [18] as we can convert (2.21) into several subproblems which can be solved efficiently. More precisely, let $d = W\chi$, $e = \mathcal{L}v$, $f = A\chi$, and $g = v$. Then (2.21) is reformulated as follows:

$$\min_{\chi,v,d,e,f,g} \frac{1}{2}\|f+g-b_l\|_\Sigma^2 + \lambda\|e\|_1 + \|\gamma\cdot d\|_{1,2}$$
$$\text{subject to } d = W\chi,\ e = \mathcal{L}v,\ f = A\chi,\ \text{and } g = v.$$

Under this reformulation, we summarize the split Bregman algorithm for (2.21) in Algorithm 1.

It is easy to see that each subproblem has a closed form solution. The solutions to (2.29) and (2.30) can be written as

$$\chi^{k+1} = \left(A^TA + I\right)^{-1}\left[A^T(f^k - r^k) + W^T(d^k - p^k)\right], \tag{2.23}$$

$$v^{k+1} = \left(I + \mathcal{L}^T\mathcal{L}\right)^{-1}\left[g^k - s^k + \mathcal{L}^T(e^k - q^k)\right]. \tag{2.24}$$

Since we use the periodic boundary conditions, both (2.23) and (2.24) can be easily solved by using the fast Fourier transform. In addition, the solutions to (2.31) and (2.32) are expressed in terms of soft thresholding:

$$d^{k+1} = \mathcal{T}_{\gamma/\beta}\left(W\chi^{k+1} + p^k\right), \tag{2.25}$$

$$e^{k+1} = \max\left(|\mathcal{L}v^{k+1} + q^k| - \lambda/\beta, 0\right)\text{sign}\left(\mathcal{L}v^{k+1} + q^k\right). \tag{2.26}$$

Here, $\mathcal{T}_\gamma$ is the isotropic soft thresholding in [4]: given d defined as

$$d = \{d_{l,\boldsymbol{\alpha}} : (l,\boldsymbol{\alpha}) \in (\{0,\dots,L-1\}\times\mathbb{B}) \cup \{(L-1,\mathbf{0})\}\}$$

and $\gamma = \{\gamma_l : l = 0,1,\dots,L-1\}$ with $\gamma_l \geq 0$, $\mathcal{T}_\gamma(d)$ is defined as

$$\left(\mathcal{T}_\gamma(d)\right)_{l,\boldsymbol{\alpha}}[\boldsymbol{k}] = \begin{cases} d_{l,\boldsymbol{\alpha}}[\boldsymbol{k}], & (l,\boldsymbol{\alpha}) = (L-1,\mathbf{0}), \\ \max\left(R_l[\boldsymbol{k}] - \gamma_l[\boldsymbol{k}], 0\right)\dfrac{d_{l,\boldsymbol{\alpha}}[\boldsymbol{k}]}{R_l[\boldsymbol{k}]}, & (l,\boldsymbol{\alpha}) \in \{0,\dots,L-1\}\times\mathbb{B}, \end{cases}$$

where $R_l[\boldsymbol{k}] = \left(\sum_{\boldsymbol{\alpha}\in\mathbb{B}} |d_{l,\boldsymbol{\alpha}}[\boldsymbol{k}]|^2\right)^{1/2}$ for $\boldsymbol{k} \in \mathbb{O}$. Finally, the solutions to (2.33) and (2.34) are expressed as

$$f^{k+1} = \left(\Sigma + \beta I\right)^{-1}\left[\Sigma(b_l - g^k) + \beta(A\chi^{k+1} + r^k)\right], \tag{2.27}$$

$$g^{k+1} = \left(\Sigma + \beta I\right)^{-1}\left[\Sigma(b_l - f^{k+1}) + \beta(v^{k+1} + s^k)\right], \tag{2.28}$$

where $\Sigma + \beta I$ is simply a diagonal matrix, and thus no matrix inversion is needed.

Note that since our model (2.21) is convex, it can be verified that Algorithm 1 converges to the minimizer of (2.21) by following the framework of [7, Theorem 3.2] whenever it has the unique global minimizer.

Algorithm 1 Split Bregman Algorithm for (2.21).

Initialization: χ^0, v^0, d^0, e^0, f^0, g^0, p^0, q^0, r^0, s^0

for $k = 0, 1, 2, \ldots$ **do**

Update χ and v:

$$\chi^{k+1} = \underset{\chi}{\operatorname{argmin}} \ \frac{\beta}{2}\|A\chi - f^k + r^k\|_2^2 + \frac{\beta}{2}\|W\chi - d^k + p^k\|_2^2, \tag{2.29}$$

$$v^{k+1} = \underset{v}{\operatorname{argmin}} \ \frac{\beta}{2}\|v - g^k + s^k\|_2^2 + \frac{\beta}{2}\|\mathcal{L}v - e^k + q^k\|_2^2. \tag{2.30}$$

Update d, e, f, and g:

$$d^{k+1} = \underset{d}{\operatorname{argmin}} \ \|\gamma \cdot d\|_{1,2} + \frac{\beta}{2}\|d - W\chi^{k+1} - p^k\|_2^2, \tag{2.31}$$

$$e^{k+1} = \underset{e}{\operatorname{argmin}} \ \lambda\|e\|_1 + \frac{\beta}{2}\|e - \mathcal{L}v^{k+1} - q^k\|_2^2, \tag{2.32}$$

$$f^{k+1} = \underset{f}{\operatorname{argmin}} \ \frac{1}{2}\|f + g^k - b_l\|_\Sigma^2 + \frac{\beta}{2}\|f - A\chi^{k+1} - r^k\|_2^2, \tag{2.33}$$

$$g^{k+1} = \underset{g}{\operatorname{argmin}} \ \frac{1}{2}\|g + f^{k+1} - b_l\|_\Sigma^2 + \frac{\beta}{2}\|g - v^{k+1} - s^k\|_2^2. \tag{2.34}$$

Update p, q, r, and s:

$$p^{k+1} = p^k + W\chi^{k+1} - d^{k+1}, \tag{2.35}$$

$$q^{k+1} = q^k + \mathcal{L}v^{k+1} - e^{k+1}, \tag{2.36}$$

$$r^{k+1} = r^k + A\chi^{k+1} - f^{k+1}, \tag{2.37}$$

$$s^{k+1} = s^k + v^{k+1} - g^{k+1}. \tag{2.38}$$

end for

3. Experimental results.

In this section, we present some experimental results on brain phantoms in [54] and in vivo MR data in [52], both of which are available on the Cornell MRI Research Lab webpage,[1] to compare the wavelet frame HIRE model (2.21) (Frame-HIRE) to several existing approaches. In this paper, we choose to compare with the TKD method (1.5) in [47], the Tikhonov regularization (1.6) in [29], the wavelet frame integral approach (Frame-Int)

$$\min_{\chi \in \mathcal{I}_3} \ \frac{1}{2}\|A\chi - b_l\|_\Sigma^2 + \|\gamma \cdot W\chi\|_{1,2}\,, \tag{3.1}$$

[1] http://www.weill.cornell.edu/mri/pages/qsm.html

and the wavelet frame differential approach (Frame-Diff)

$$\min_{\chi\in\mathcal{I}_3}\ \frac{1}{2}\left\|\mathcal{L}A\chi-\mathcal{L}b_l\right\|_\Sigma^2+\left\|\gamma\cdot W\chi\right\|_{1,2}, \tag{3.2}$$

where the signal-to-noise ratio (SNR) weight for (3.2) is estimated by the method described in [27]. Moreover, in order to highlight the main focus of this paper—to propose a two-system regularization model by identifying a harmonic incompatibility in the measured local field data—we also test the models by placing $\|\gamma\cdot W\chi\|_{1,2}$ in (2.21), (3.1), and (3.2) into the following TGV term:

$$\mathrm{TGV}^2_{\alpha_1,\alpha_0}(\chi)=\alpha_1\left\|\nabla\chi-p\right\|_1+\alpha_0\left\|\mathcal{E}p\right\|_1,\quad \text{where}\ \ \mathcal{E}=\frac{1}{2}\left(\nabla+\nabla^T\right), \tag{3.3}$$

which will be denoted by TGV-HIRE, TGV-Int, and TGV-Diff, respectively. All experiments are implemented on MATLAB R2015a running on a platform with 16GB RAM and Intel Xeon CPU E5-2609 0 at 2.40GHz with 4 cores.

In (2.21), (3.1), and (3.2), we choose W to be the tensor product Haar framelet transform with 1 level of decomposition to avoid a memory storage problem. Note, however, that the decomposition level and the choice of W will affect the restoration results. In addition, we use the standard difference for the TGV term and the standard centered difference for $\mathcal{L}$ in the HIRE approaches. The stopping criterion for Algorithm 1 is

$$\frac{\|\chi^{k+1}-\chi^k\|_2}{\|\chi^{k+1}\|_2}\le 5\times 10^{-3},$$

and (3.1) and (3.2) as well as the TGV models are solved using the split Bregman algorithm presented in [7, 22], with the same stopping criterion as above. For the parameters, we choose γ in (2.22) as $\gamma=\left\{\nu 2^{-l}: l=0,\dots,L-1\right\}$ with $\nu>0$ according to [4]. Empirically, we observe that $\alpha_0=2\alpha_1$ for (3.3), $\lambda=5\nu$ for Frame-HIRE, and $\lambda=8\alpha_1$ for TGV-HIRE are good choices. Parameters ν and α_1 vary case by case, and are chosen manually to promote an optimal balance between indices and visual qualities; even though the parameters have few effects on the indices, the reconstructed images contain more and more artifacts as the parameters become smaller. Finally, we compute the root mean square error (RMSE), the structural similarity index map (SSIM) [53], and the computation time of the brain phantom experimental results for a quantitative comparison of each reconstruction model.

3.1. Experiments on brain phantom. For the brain phantom experiments, we use a $256\times256\times98$ image with spatial resolution $0.9375\times0.9375\times1.5\mathrm{mm}^3$ to simulate the 11 equispaced multiecho GREs at 3T with TE ranging from 2.6msec to 28.6msec. We first simulate the true total field by adding four background susceptibility sources in the true susceptibility image to provide the background field. Then we generate the multiecho complex GRE signal by

$$I(\boldsymbol{k},t)=\widetilde{m}(\boldsymbol{k})\exp\left\{-i\widetilde{b}(\boldsymbol{k})\omega_0B_0TE(t)\right\},\qquad \boldsymbol{k}\in\mathbb{O}\ \ \text{and}\ \ t=1,\dots,11,$$

with a given true magnitude image $\widetilde{m}$ and true total field $\widetilde{b}$. Then the white Gaussian noise with standard deviation 0.02 is added to both the real and the complex part of each GRE

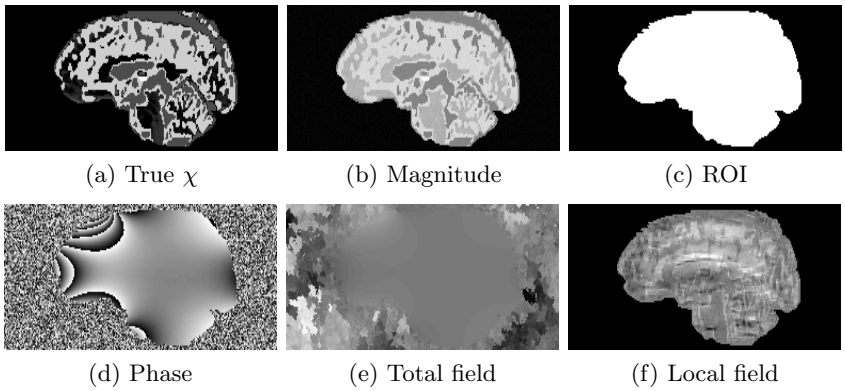

(a) True χ (b) Magnitude (c) ROI

(d) Phase (e) Total field (f) Local field

Figure 6. *Sagittal slice images of synthesized data sets for the brain phantom experiments.*

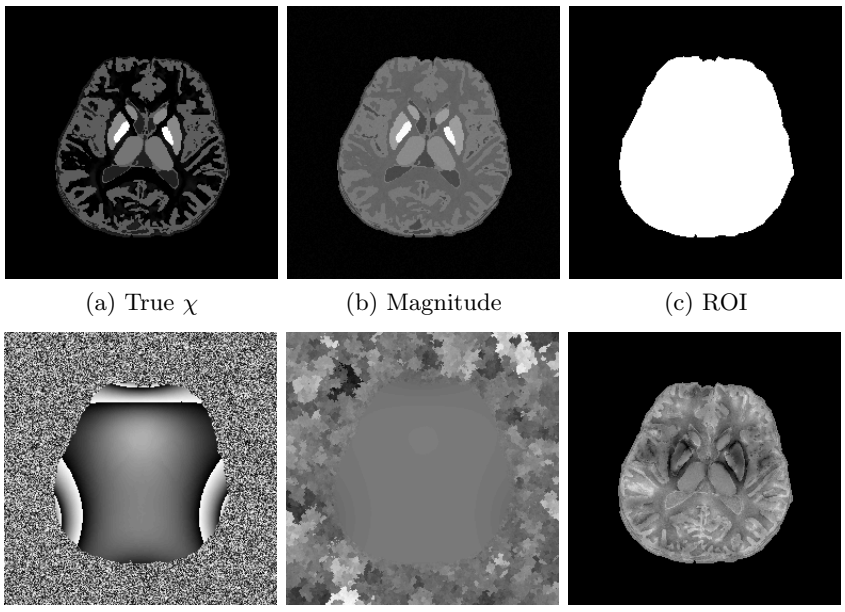

(a) True χ (b) Magnitude (c) ROI

(d) Phase (e) Total field (f) Local field

Figure 7. *Axial slice images of synthesized data sets for the brain phantom experiments.*

signal. Using the simulated noisy multiecho GRE signal, we estimate the magnitude image and phase data using the method in [12], and the phase is further unwrapped by the method in [21] to obtain the noisy and incomplete total field b. Finally, we solve the Poisson equation (2.10) using the method in [57] to obtain the noisy local field data b_l. (See Figures 6 and 7.)

All regularization-based models are initialized with $\chi^0 = 0$, and both Frame-HIRE and TGV-HIRE are also initialized with $v^0 = 0$. For the parameters, we choose $\hbar = 0.125$ for (1.5), $\varepsilon = 0.01$ for (1.6), $\nu = 0.0005$ for Frame-Int and Frame-HIRE, $\nu = 0.004$ for Frame-Diff, $\alpha_1 = 0.00025$ for TGV-Int and TGV-HIRE, and $\alpha_1 = 0.002$ for TGV-Diff. In addition, we

Table 1

Comparison of relative error, and structural similarity index map, for the direct approaches and the wavelet frame regularization approach in the brain phantom experiments. Boldface numbers indicate the best result.

Indices	Direct approach		Regularization		
	TKD	Tikhonov	Integral	Differential	HIRE
RMSE	0.5579	0.5546	0.4516	0.6143	**0.4183**
SSIM	0.6546	0.6474	0.7485	0.6188	**0.7586**

choose $\beta = 0.05$ for all split Bregman algorithms to solve the regularization-based models including Algorithm 1.

Table 1 summarizes the relative error and the SSIM of the direct approaches ((1.5) and (1.6)) and the wavelet frame regularization approaches, and Figures 8 and 9 present visual comparisons of the results. In addition, Table 2 summarizes the aforementioned indices of the direct approaches and the TGV regularization approaches, and Figures 10 and 11 depict the visual comparisons. We can see that both Frame-HIRE and TGV-HIRE consistently outperform the existing direct approaches, the integral approaches, and the differential approaches in both cases. At first glance, this verifies the convention that the regularization-based models in general perform better in solving the ill-posed inverse problem of QSM than the direct methods [27, 51]. Most importantly, this result demonstrates that the measured local field data obtained from the phase of a complex GRE MR signal contains harmonic incompatibility other than the noise, which agrees with our theoretical discovery, and the performance gain mainly comes from taking both the noise in the measured data and the harmonic incompatibility (the incompatibility other than the noise) at the same time. Meanwhile, since this harmonic incompatibility is not taken into account in the integral approaches, the reconstructed susceptibility images contain the shadow artifacts as shown in Figures 8(d), 9(d), 10(d), and 11(d). The differential approaches can remove the harmonic incompatibility in the measured data in advance, leading to the shadow artifact removal compared to the integral approach. However, since the noise in b_l was amplified by $\mathcal{L}$, the final reconstructed images contain the streaking artifacts as shown in Figures 8(e), 9(e), 10(e), and 11(e), leading to the degradation in indices at the same time.

Finally, we mention that even though TGV-HIRE performs slightly better than Frame-HIRE from the viewpoint of indices, compared to Frame-HIRE in Figures 8(f) and 9(f), the TGV-HIRE yields an overly smoothed restoration result, as shown in Figures 10(f) and 11(f). In addition, since $\mathcal{D}(\mathbf{0}) = 0$, the χ subproblem of TGV-HIRE has a rank deficient system matrix due to the constant offset, unlike Frame-HIRE, whose system matrix has a full column rank due to $W^T W = I$. As a consequence, the CPU time of TGV-HIRE becomes approximately 3 times longer than the approximately 11.5 minutes of Frame-HIRE, as shown in Table 3, which shows that the TGV regularization approach may not be suitable for real clinical applications. Therefore, even though it is approximately 1.9 times slower than Frame-Int, we can nevertheless conclude that, compared to TGV-HIRE, Frame-HIRE is able to achieve the efficiency of its split Bregman algorithm as well as the shadow and streaking artifact removal.

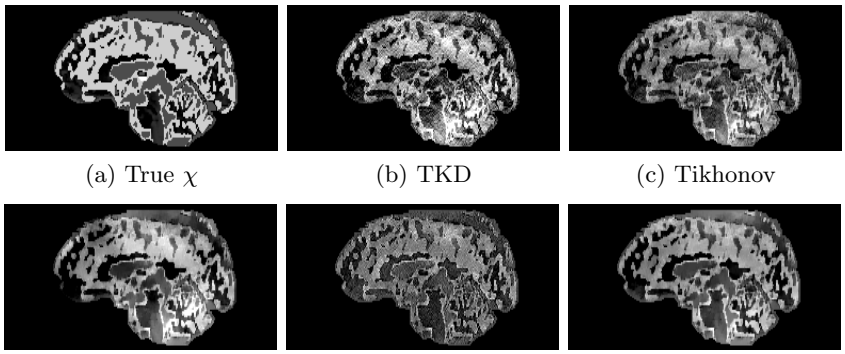

(a) True χ (b) TKD (c) Tikhonov

(d) Frame-Int (e) Frame-Diff (f) Frame-HIRE

Figure 8. *Sagittal slice images comparing QSM reconstruction methods for the brain phantom experiments. All sagittal slice images of brain phantom experimental results are displayed in the window level* $[-0.03, 0.07]$ *for a fair comparison.*

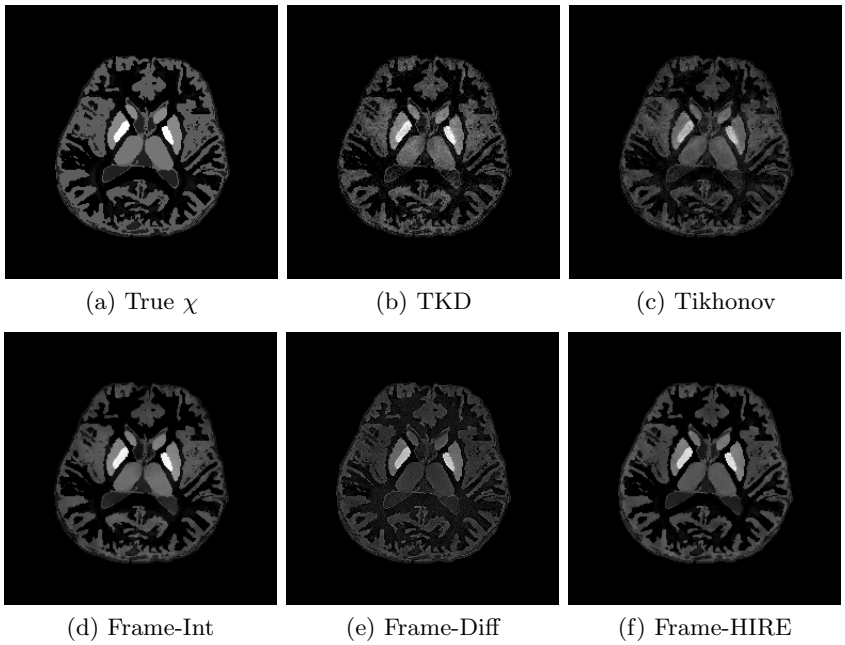

(a) True χ (b) TKD (c) Tikhonov

(d) Frame-Int (e) Frame-Diff (f) Frame-HIRE

Figure 9. *Axial slice images comparing QSM reconstruction methods for the brain phantom experiments with the wavelet frame regularization. All axial slice images of brain phantom experimental results are displayed in the window level* $[-0.03, 0.19]$ *for a fair comparison.*

3.2. Experiments on in vivo MR data. The in vivo MR data experiments are conducted using a $256 \times 256 \times 146$ image with spatial resolution $0.9375 \times 0.9375 \times 1\text{mm}^3$ which can be downloaded from the Cornell MRI Research Lab webpage. Using the wrapped phase image presented in Figures 12(c) and 13(c), we unwrap the phase using the method in [21] to obtain the total field b in Figures 12(d) and 13(d). Then the measured local field data b_l in

Table 2

Comparison of relative error, and structural similarity index map for the direct approaches and the TGV regularization approach in the brain phantom experiments. Boldface numbers indicate the best result.

Indices	Direct approach		Regularization		
	TKD	Tikhonov	Integral	Differential	HIRE
RMSE	0.5579	0.5546	0.4129	0.4568	**0.3589**
SSIM	0.6546	0.6474	0.7861	0.7147	**0.7903**

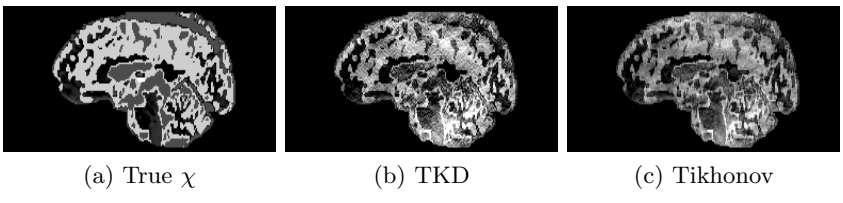

(a) True χ (b) TKD (c) Tikhonov

(d) TGV-Int (e) TGV-Diff (f) TGV-HIRE

Figure 10. *Sagittal slice images comparing QSM reconstruction methods for the brain phantom experiments with the TGV regularization. All sagittal slice images of brain phantom experimental results are displayed in the window level* $[-0.03, 0.07]$ *for a fair comparison.*

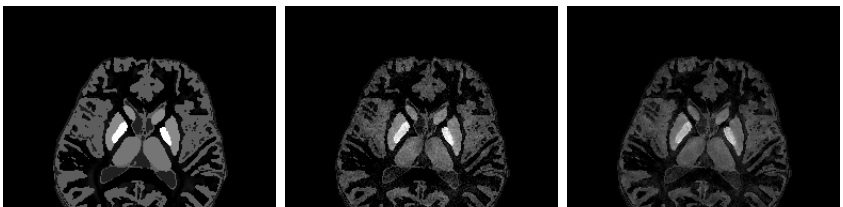

(a) True χ (b) TKD (c) Tikhonov

(d) TGV-Int (e) TGV-Diff (f) TGV-HIRE

Figure 11. *Axial slice images comparing QSM reconstruction methods for the brain phantom experiments with the TGV regularization. All axial slice images of brain phantom experimental results are displayed in the window level* $[-0.03, 0.19]$ *for a fair comparison.*

Table 3

Comparison of the CPU time for the brain phantom with respect to the choice of regularization term.

Indices	Wavelet frame			TGV		
	Integral	Differential	HIRE	Integral	Differential	HIRE
CPU time	366.55	350.33	685.32	1327.66	365.42	2020.29

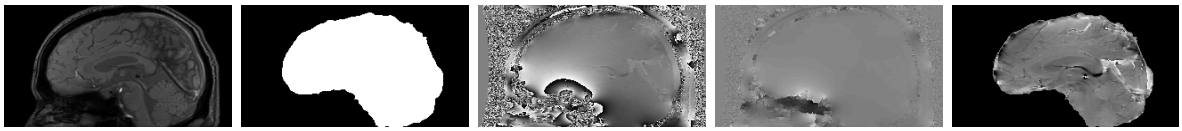

(a) Magnitude (b) ROI (c) Phase (d) Total field (e) Local field

Figure 12. *Sagittal slice images of data sets for the in vivo MR data experiments.*

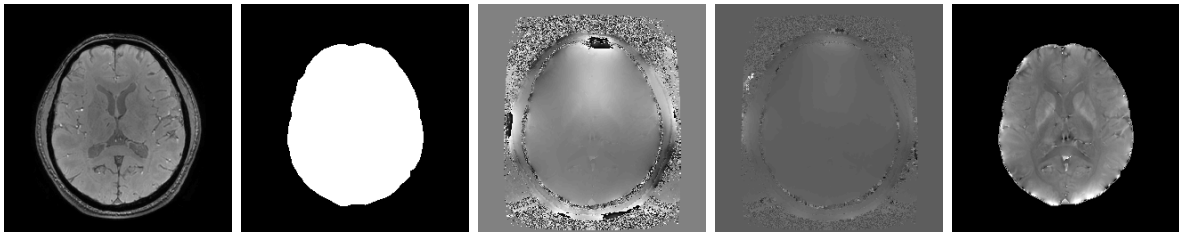

(a) Magnitude (b) ROI (c) Phase (d) Total field (e) Local field

Figure 13. *Axial slice images of data sets for the in vivo MR data experiments.*

Figures 12(e) and 13(e) is obtained by solving the Poisson equation (2.10) using the method in [57].

As in subsection 3.1, all regularization-based models are initialized with $\chi^0 = 0$, and both Frame-HIRE and TGV-HIRE are also initialized with $v^0 = 0$. For the parameters, we choose $\hbar = 0.1$ for (1.5), $\varepsilon = 0.01$ for (1.6), $\nu = 0.0005$ for Frame-Int and Frame-HIRE, $\nu = 0.005$ for Frame-Diff, $\alpha_1 = 0.00025$ for TGV-Int and TGV-HIRE, and $\alpha_1 = 0.0025$ for TGV-Diff. In addition, we choose $\beta = 0.05$ for all split Bregman algorithms to solve the regularization-based models including Algorithm 1.

Figures 14 and 15 display the visual comparisons of the direct approaches and the wavelet frame regularization approaches, and the zoom-in views of Figure 14 are provided in Figure 16. We also provide visual comparisons of the direct approaches and the TGV regularization approaches in Figures 17 to 19. Since the reference image is not available for in vivo MR data, it is in general more difficult to provide quantitative evaluations than for the numerical brain phantom. Nonetheless, we can see from the viewpoint of visual comparison that the pros and cons are almost the same as the numerical brain phantom experiments. It is also worth noting that the HIRE models can reduce the streaking artifacts which propagate from $\partial\Omega$ into Ω as well as the shadow artifacts. As pointed out in [52], the in vivo local field data is prone to outliers near $\partial\Omega$ because the GRE signal lacks information outside Ω. Hence, we can see that most streaking artifacts propagate from these outliers near $\partial\Omega$ into the ROI. However, thanks

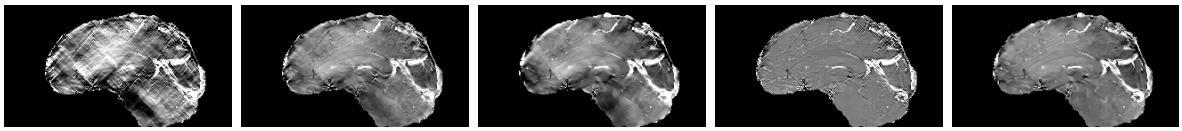

(a) TKD (b) Tikhonov (c) Frame-Int (d) Frame-Diff (e) Frame-HIRE

Figure 14. *Sagittal slice images comparing QSM reconstruction methods for the in vivo MR data experiments with the wavelet frame regularization. All images of in vivo MR data experimental results are displayed in the window level* $[-0.2, 0.2]$ *for a fair comparison.*

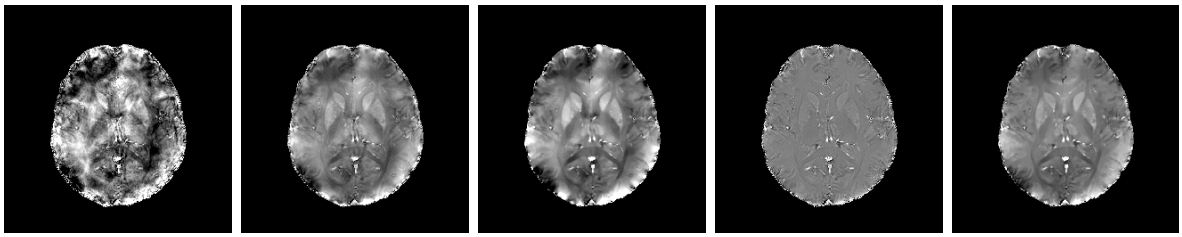

(a) TKD (b) Tikhonov (c) Frame-Int (d) Frame-Diff (e) Frame-HIRE

Figure 15. *Axial slice images comparing QSM reconstruction methods for the in vivo MR data experiments with the wavelet frame regularization.*

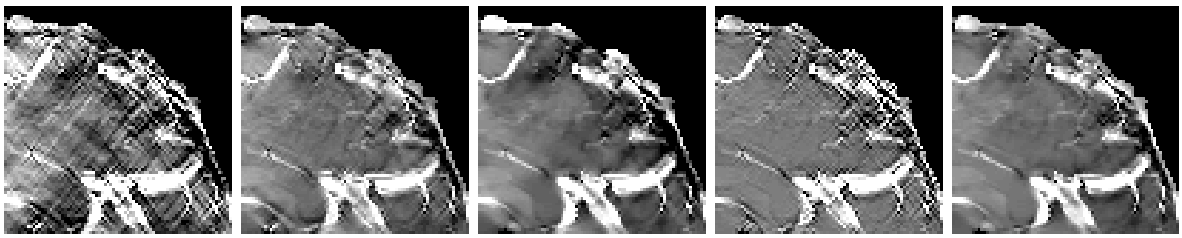

(a) TKD (b) Tikhonov (c) Frame-Int (d) Frame-Diff (e) Frame-HIRE

Figure 16. *Zoom-in views of Figure 14.*

to the sparsity promoting property of the ℓ_1 norm, the term $\lambda \|\mathcal{L}v\|_1$ in the HIRE approaches can somehow capture and remove them, leading to the suppression of artifacts propagating from $\partial\Omega$ into Ω as well as the shadow and streaking artifact removal. Finally, even though we may also note that the Tikhonov regularization can somehow reduce the artifacts, there is some loss of features due to the smoothness prior of the susceptibility image.

Finally, similar to the brain phantom experiments, TGV-HIRE restores an overly smoothed susceptibility image as shown in Figures 17(e), 18(e), and 19(e), compared to Frame-HIRE in Figures 14(e), 15(e), and 16(e). In addition, the split Bregman algorithm of TGV-HIRE is approximately 7 times slower than Frame-HIRE, as shown in Table 4, which again shows that the TGV regularization approach may not be suitable for real clinical applications. Hence, as in the brain phantom experiments, we can conclude that, compared to TGV-HIRE, Frame-HIRE is able to achieve the efficiency of its split Bregman algorithm as well as the shadow and streaking artifact removal.

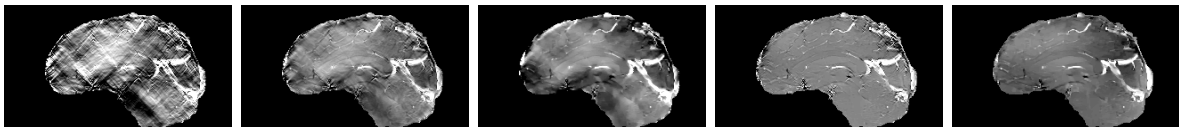

(a) TKD (b) Tikhonov (c) TGV-Int (d) TGV-Diff (e) TGV-HIRE

Figure 17. *Sagittal slice images comparing QSM reconstruction methods for the in vivo MR data experiments with TGV regularization. All images of in vivo MR data experimental results are displayed in the window level* $[-0.2, 0.2]$ *for a fair comparison.*

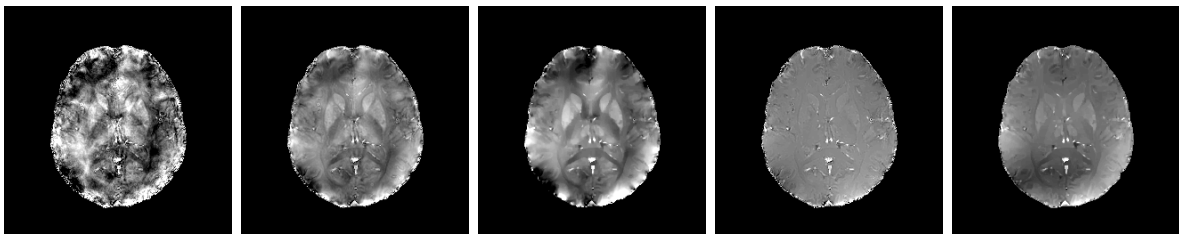

(a) TKD (b) Tikhonov (c) TGV-Int (d) TGV-Diff (e) TGV-HIRE

Figure 18. *Axial slice images comparing QSM reconstruction methods for the in vivo MR data experiments with TGV regularization.*

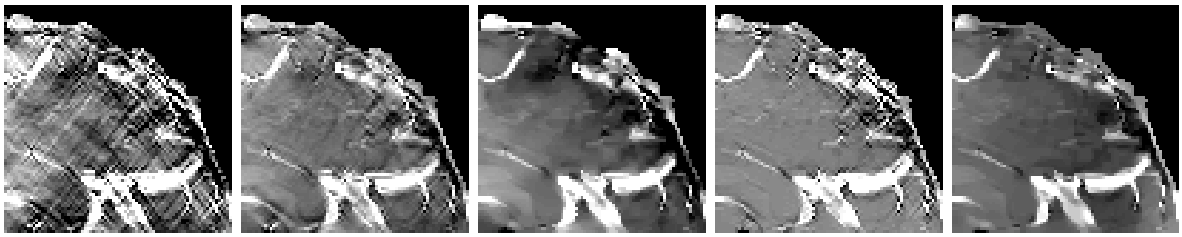

(a) TKD (b) Tikhonov (c) TGV-Int (d) TGV-Diff (e) TGV-HIRE

Figure 19. *Zoom-in views of Figure 17.*

Table 4

Comparison of the CPU time for the in vivo data with respect to the choice of regularization term.

Indices	Wavelet frame			TGV		
	Integral	Differential	HIRE	Integral	Differential	HIRE
CPU time	628.25	353.32	953.10	3330.51	775.60	6776.12

4. Conclusion. In this paper, we proposed a new regularization-based susceptibility reconstruction model. The proposed HIRE model is based on the identification of the harmonic incompatibility in the measured local field data arising from the underlying PDE (1.8). The harmonic property is imposed as a prior of incompatibility via the sparsity under the Laplacian into the integral approach so that we can apply the idea of a two-system regularization model. By doing so, we can take into account the incompatibility in the data which is other than the additive noise, achieving the susceptibility image reconstruction with fewer artifacts.

Finally, the experimental results show that our proposed approach (2.21) outperforms the existing approaches in both brain phantom and in vivo MR data.

Appendix A. Preliminaries on wavelet frame. Provided here is a brief introduction to the tight wavelet frame. Briefly speaking, it is a generalization of the orthogonal wavelet basis (see, e.g., [37]) to the redundant system, and due to the redundancy, it is more robust to errors than the traditional orthonormal basis [17]. Interested readers may consult [10, 11, 41] for frame and wavelet frame theories, [46] for a short survey on the theory and applications of frames, and [15, 16] for more detailed surveys.

For a given $\boldsymbol{\Psi} = \{\psi_1, \dots, \psi_r\} \subseteq L_2(\mathbb{R}^d)$ with $d \in \mathbb{N}$, a quasi-affine system $\mathcal{X}(\boldsymbol{\Psi})$ generated by $\boldsymbol{\Psi}$ is the collection of the dilations and the shifts of the elements in $\boldsymbol{\Psi}$:

$$\mathcal{X}(\boldsymbol{\Psi}) = \left\{ \psi_{\alpha,n,\boldsymbol{k}} : 1 \le \alpha \le r,\ n \in \mathbb{Z},\ \boldsymbol{k} \in \mathbb{Z}^d \right\}, \tag{A.1}$$

where $\psi_{\alpha,n,\boldsymbol{k}}$ is defined as

$$\psi_{\alpha,n,\boldsymbol{k}} = \begin{cases} 2^{\frac{nd}{2}} \psi_\alpha(2^n \cdot - \boldsymbol{k}), & n \ge 0, \\ 2^{nd} \psi_\alpha(2^n \cdot - 2^n \boldsymbol{k}), & n < 0. \end{cases} \tag{A.2}$$

We say that $\mathcal{X}(\boldsymbol{\Psi})$ is a tight wavelet frame on $L_2(\mathbb{R}^d)$ if we have

$$\|f\|^2_{L_2(\mathbb{R}^d)} = \sum_{\alpha=1}^{r} \sum_{n\in\mathbb{Z}} \sum_{\boldsymbol{k}\in\mathbb{Z}^d} |\langle f, \psi_{\alpha,n,\boldsymbol{k}} \rangle|^2 \tag{A.3}$$

for every $f \in L_2(\mathbb{R}^d)$. In this case, each ψ_α is called a (tight) framelet, and $\langle f, \psi_{\alpha,n,\boldsymbol{k}} \rangle$ is called the canonical coefficient of f.

The constructions of (anti)symmetric and compactly supported framelets $\boldsymbol{\Psi}$ are usually based on a multiresolution analysis (MRA); we first find some compactly supported refinable function ϕ with a refinement mask q_0 such that

$$\phi = 2^d \sum_{\boldsymbol{k}\in\mathbb{Z}^d} q_0[\boldsymbol{k}] \phi(2 \cdot - \boldsymbol{k}). \tag{A.4}$$

Then the MRA-based construction of $\boldsymbol{\Psi} = \{\psi_1, \dots, \psi_r\} \subseteq L_2(\mathbb{R}^d)$ is to find finitely supported masks q_α such that

$$\psi_\alpha = 2^d \sum_{\boldsymbol{k}\in\mathbb{Z}^d} q_\alpha[\boldsymbol{k}] \phi(2 \cdot - \boldsymbol{k}), \qquad \alpha = 1, \dots, r. \tag{A.5}$$

The sequences $q_1, \dots, q_r$ are called the wavelet frame mask or the high pass filters of the system, and the refinement mask q_0 is also called the low pass filter.

The unitary extension principle (UEP) of [41] provides a general theory of the construction of MRA-based tight wavelet frames. Briefly speaking, as long as $\{q_0, q_1, \dots, q_r\}$ are compactly supported and their Fourier series $\widehat{q}_\alpha(\boldsymbol{\xi}) = \sum_{\boldsymbol{k}\in\mathbb{Z}^d} q_\alpha[\boldsymbol{k}] e^{-i\boldsymbol{\xi}\cdot\boldsymbol{k}}$ satisfy

$$\sum_{\alpha=0}^{r} |\widehat{q}_\alpha(\boldsymbol{\xi})|^2 = 1 \quad \text{and} \quad \sum_{\alpha=0}^{r} \widehat{q}_\alpha(\boldsymbol{\xi}) \overline{\widehat{q}_\alpha(\boldsymbol{\xi} + \boldsymbol{\nu})} = 0 \tag{A.6}$$

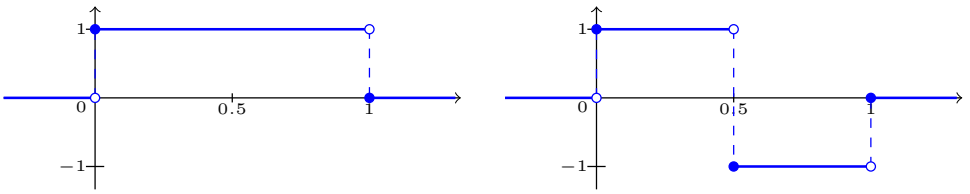

(a) Refinable function ϕ (b) Framelet function ψ_1

Figure 20. *Illustration of ϕ and ψ_1 in Example A.1.*

for all $\boldsymbol{\nu} \in \{0,\pi\}^d \setminus \{\mathbf{0}\}$ and $\boldsymbol{\xi} \in [-\pi,\pi]^d$, the quasi-affine system $\mathcal{X}(\boldsymbol{\Psi})$ with $\boldsymbol{\Psi} = \{\psi_1,\dots,\psi_r\}$ defined by (A.5) forms a tight frame of $L_2(\mathbb{R}^d)$, and the filters $\{q_0, q_1, \dots, q_r\}$ form a discrete tight frame on $\ell_2(\mathbb{Z}^d)$ [15].

Example A.1. The piecewise constant B-spline (or the Haar framelet) [11] for $L_2(\mathbb{R})$ has one refinable function and one framelet,

$$\phi(x) = \begin{cases} 1 & \text{if} \quad x \in [0,1), \\ 0 & \text{if} \quad x \notin [0,1) \end{cases} \qquad \text{and} \qquad \psi_1(x) = \begin{cases} 1 & \text{if} \quad x \in [0,1/2), \\ -1 & \text{if} \quad x \in [1/2,1), \\ 0 & \text{if} \quad x \notin [0,1), \end{cases}$$

as shown in Figure 20. Here, the associated filters are

$$q_0 = \frac{1}{2}\begin{bmatrix} 1 & 1 \end{bmatrix} \quad \text{and} \quad q_1 = \frac{1}{2}\begin{bmatrix} 1 & -1 \end{bmatrix}.$$

Since this $\{q_0, q_1\}$ satisfies (A.6), $\mathcal{X}(\boldsymbol{\Psi})$ with $\boldsymbol{\Psi} = \{\psi_1\}$ forms a tight frame on $L_2(\mathbb{R})$.

The tight frame on $L_2(\mathbb{R}^d)$ with $d \geq 2$ can be constructed by taking tensor products of univariate tight framelets [4, 5, 10, 15]. Given a set of univariate masks $\{q_0, q_1, \dots, q_r\}$, we define multivariate masks $q_{\boldsymbol{\alpha}}[\boldsymbol{k}]$ with $\boldsymbol{\alpha} = (\alpha_1,\dots,\alpha_d)$ and $\boldsymbol{k} = (k_1,\dots,k_d)$ as

$$q_{\boldsymbol{\alpha}}[\boldsymbol{k}] = q_{\alpha_1}[k_1] \cdots q_{\alpha_d}[k_d], \qquad 0 \leq \alpha_1,\dots,\alpha_d \leq r, \quad \boldsymbol{k} = (k_1,\dots,k_d) \in \mathbb{Z}^d.$$

The corresponding multivariate refinable function and framelets are defined as

$$\psi_{\boldsymbol{\alpha}}(\boldsymbol{x}) = \psi_{\alpha_1}(x_1) \cdots \psi_{\alpha_d}(x_d), \qquad 0 \leq \alpha_1,\dots,\alpha_d \leq r, \quad \boldsymbol{x} = (x_1,\dots,x_d) \in \mathbb{R}^d,$$

with $\psi_0 = \phi$ for convenience. If the univariate masks $\{q_\alpha\}$ are constructed from UEP, then we can verify that $\{q_{\boldsymbol{\alpha}}\}$ satisfies (A.6) and thus $\mathcal{X}(\boldsymbol{\Psi})$ with $\boldsymbol{\Psi} = \{\psi_{\boldsymbol{\alpha}} : \boldsymbol{\alpha} \in \{0,\dots,r\}^d \setminus \{\mathbf{0}\}\}$ forms a tight frame for $L_2(\mathbb{R}^d)$.

In the discrete setting, let $\mathcal{I}_d \simeq \mathbb{R}^{N_1 \times \cdots \times N_d}$ be the space of real-valued functions defined on a regular grid $\{0,1,\dots,N_1-1\} \times \cdots \times \{0,1,\dots,N_d-1\}$. The fast framelet decomposition, or the analysis operator with L levels of decomposition, is defined as

$$Wu = \{W_{l,\boldsymbol{\alpha}} u : (l,\boldsymbol{\alpha}) \in (\{0,\dots,L-1\} \times \mathbb{B}) \cup \{(L-1,\mathbf{0})\}\}, \tag{A.7}$$

where $\mathbb{B} = \{0, \dots, r\}^d \setminus \{\mathbf{0}\}$ is the framelet band. Then the frame coefficients $W_{l,\boldsymbol{\alpha}} u \in \mathcal{I}_d$ of $u \in \mathcal{I}_d$ at level l and band $\boldsymbol{\alpha}$ are defined as

$$W_{l,\boldsymbol{\alpha}} u = q_{l,\boldsymbol{\alpha}}[-\cdot] \circledast u,$$

where $\circledast$ denotes the discrete convolution with a certain boundary condition (e.g., the periodic boundary condition), and $q_{l,\boldsymbol{\alpha}}$ is defined as

$$q_{l,\boldsymbol{\alpha}} = \widetilde{q}_{l,\boldsymbol{\alpha}} \circledast \widetilde{q}_{l-1,\mathbf{0}} \circledast \cdots \circledast \widetilde{q}_{0,\mathbf{0}} \quad \text{with} \quad \widetilde{q}_{l,\boldsymbol{\alpha}}[\boldsymbol{k}] = \begin{cases} q_{\boldsymbol{\alpha}}[2^{-l}\boldsymbol{k}], & \boldsymbol{k} \in 2^l \mathbb{Z}^d, \\ 0, & \boldsymbol{k} \notin 2^l \mathbb{Z}^d. \end{cases} \tag{A.8}$$

We denote by W^T, the adjoint of W, the fast reconstruction (or the synthesis operator). Then by UEP (A.6), we have $W^T W = I$.

Finally, we mention that among many different choices of framelets, the ones constructed from the B-spline are the most popular in image processing. This is due to the multiscale structure of the wavelet frame systems, short supports of the (anti)symmetric framelet functions with varied vanishing moments, and the presence of both low pass and high pass filters in the wavelet frame filter banks, which are desirable in sparsely approximating images [17]. A tight frame system constructed from the low order B-spline has fewer filters with shorter supports compared to the ones constructed from the high order B-splines. Hence, low order B-spline framelet systems are more computationally efficient, while the high order ones are capable of capturing richer image singularities. Moreover, since high order B-spline framelets have larger supports, they may introduce more numerical viscosity, often leading to smoother reconstructions in image restoration tasks. Hence, the choice of framelet systems indeed depends on the task and the computational cost we can afford [56]. In this paper, we fix W to be the Haar framelet system for the wavelet frame regularization models as the susceptibility images can be well approximated by piecewise constant functions. In addition, we always fix $L = 1$ to avoid memory storage problems, as we are solving a three-dimensional inverse problem. We also note that the choices of W will indeed affect the reconstruction results. For example, the use of data driven tight frames in [6] will generate better reconstruction results due to its adaptivity, even though it requires further numerical studies. Nonetheless, we forgo further details on the choice of W in order not to dilute the main focus of this paper.

Acknowledgments. We thank the authors of [52, 54] for making the data sets and the MATLAB toolbox available so that the experiments could be implemented. We also thank the anonymous reviewers for their constructive suggestions and comments that helped tremendously with improving the presentation of the paper.

REFERENCES

[1] J. Acosta-Cabronero, G. B. Williams, A. Cardenas-Blanco, R. J. Arnold, V. Lupson, and P. J. Nestor, *In vivo quantitative susceptibility mapping (QSM) in Alzheimer's disease*, PloS One, 8 (2013), e81093, https://doi.org/10.1371/journal.pone.0081093.

[2] K. Bredies, K. Kunisch, and T. Pock, *Total generalized variation*, SIAM J. Imaging Sci., 3 (2010), pp. 492–526, https://doi.org/10.1137/090769521.

[3] J. F. Cai, R. H. Chan, and Z. Shen, *Simultaneous cartoon and texture inpainting*, Inverse Probl. Imaging, 4 (2010), pp. 379–395, https://doi.org/10.3934/ipi.2010.4.379.

[4] J. F. Cai, B. Dong, S. Osher, and Z. Shen, *Image restoration: Total variation, wavelet frames, and beyond*, J. Amer. Math. Soc., 25 (2012), pp. 1033–1089, https://doi.org/10.1090/S0894-0347-2012-00740-1.
[5] J. F. Cai, B. Dong, and Z. Shen, *Image restoration: A wavelet frame based model for piecewise smooth functions and beyond*, Appl. Comput. Harmon. Anal., 41 (2016), pp. 94–138, https://doi.org/10.1016/j.acha.2015.06.009.
[6] J. F. Cai, H. Ji, Z. Shen, and G. B. Ye, *Data-driven tight frame construction and image denoising*, Appl. Comput. Harmon. Anal., 37 (2014), pp. 89–105, https://doi.org/10.1016/j.acha.2013.10.001.
[7] J.-F. Cai, S. Osher, and Z. Shen, *Split Bregman methods and frame based image restoration*, Multiscale Model. Simul., 8 (2009), pp. 337–369, https://doi.org/10.1137/090753504.
[8] W. Chen, S. A. Gauthier, A. Gupta, J. Comunale, T. Liu, S. Wang, M. Pei, D. Pitt, and Y. Wang, *Quantitative susceptibility mapping of multiple sclerosis lesions at various ages*, Radiology, 271 (2014), pp. 183–192, https://doi.org/10.1148/radiol.13130353.
[9] J. K. Choi, H. S. Park, S. Wang, Y. Wang, and J. K. Seo, *Inverse problem in quantitative susceptibility mapping*, SIAM J. Imaging Sci., 7 (2014), pp. 1669–1689, https://doi.org/10.1137/140957433.
[10] I. Daubechies, *Ten Lectures on Wavelets*, CBMS-NSF Regional Conf. Ser. in Appl. Math. 61, SIAM, Philadelphia, 1992, https://doi.org/10.1137/1.9781611970104.
[11] I. Daubechies, B. Han, A. Ron, and Z. Shen, *Framelets: MRA-based constructions of wavelet frames*, Appl. Comput. Harmon. Anal., 14 (2003), pp. 1–46, https://doi.org/10.1016/S1063-5203(02)00511-0.
[12] L. de Rochefort, R. Brown, M. R. Prince, and Y. Wang, *Quantitative MR susceptibility mapping using piece-wise constant regularized inversion of the magnetic field*, Magn. Reson. Med., 60 (2008), pp. 1003–1009, https://doi.org/10.1002/mrm.21710.
[13] L. de Rochefort, T. Liu, B. Kressler, J. Liu, P. Spincemaille, V. Lebon, J. Wu, and Y. Wang, *Quantitative susceptibility map reconstruction from MR phase data using bayesian regularization: Validation and application to brain imaging*, Magn. Reson. Med., 63 (2010), pp. 194–206, https://doi.org/10.1002/mrm.22187.
[14] A. V. Dimov, Z. Liu, P. Spincemaille, M. R. Prince, J. Du, and Y. Wang, *Bone quantitative susceptibility mapping using a chemical species-specific R2* signal model with ultrashort and conventional echo data*, Magn. Reson. Med., 79 (2018), pp. 121–128, https://doi.org/10.1002/mrm.26648.
[15] B. Dong and Z. Shen, *MRA-based wavelet frames and applications*, in Mathematics in Image Processing, IAS/Park City Math. Ser. 19, AMS, Providence, RI, 2013, pp. 9–158.
[16] B. Dong and Z. Shen, *Image restoration: A data-driven perspective*, in Proceedings of the 8th International Congress on Industrial and Applied Mathematics, Higher Ed. Press, Beijing, 2015, pp. 65–108.
[17] B. Dong, Z. Shen, and P. Xie, *Image restoration: A general wavelet frame based model and its asymptotic analysis*, SIAM J. Math. Anal., 49 (2017), pp. 421–445, https://doi.org/10.1137/16M1064969.
[18] J. Eckstein and D. P. Bertsekas, *On the Douglas-Rachford splitting method and the proximal point algorithm for maximal monotone operators*, Math. Programming, 55 (1992), pp. 293–318, https://doi.org/10.1007/BF01581204.
[19] L. C. Evans, *Partial Differential Equations*, 2nd ed., Grad. Stud. Math. 19, AMS, Providence, RI, 2010, https://doi.org/10.1090/gsm/019.
[20] M. W. Gee, J. J. Hu, and R. S. Tuminaro, *A new smoothed aggregation multigrid method for anisotropic problems*, Numer. Linear Algebra Appl., 16 (2009), pp. 19–37, https://doi.org/10.1002/nla.593.
[21] D. C. Ghiglia and M. D. Pritt, *Two-Dimensional Phase Unwrapping: Theory, Algorithms, and Software*, Wiley-Interscience, New York, 1998.
[22] W. Guo, J. Qin, and W. Yin, *A new detail-preserving regularization scheme*, SIAM J. Imaging Sci., 7 (2014), pp. 1309–1334, https://doi.org/10.1137/120904263.
[23] E. M. Haacke, R. W. Brown, M. R. Thompson, and R. Venkatesan, *Magnetic Resonance Imaging: Physical Principles and Sequence Design*, 1st ed., Wiley, New York, 1999.
[24] E. M. Haacke, S. Liu, S. Buch, W. Zheng, D. Wu, and Y. Ye, *Quantitative susceptibility mapping: Current status and future directions*, Magn. Reson. Imaging, 33 (2015), pp. 1–25, https://doi.org/10.1016/j.mri.2014.09.004.
[25] E. M. Haacke, J. Tang, J. Neelavalli, and Y. C. N. Cheng, *Susceptibility mapping as a means to visualize veins and quantify oxygen saturation*, J. Magn. Reson. Imag., 32 (2010), pp. 663–676, https://doi.org/10.1002/jmri.22276.

[26] Y. Kee, J. Cho, K. Deh, Z. Liu, P. Spincemaille, and Y. Wang, *Coherence enhancement in quantitative susceptibility mapping by means of anisotropic weighting in morphology enabled dipole inversion*, Magn. Reson. Med., 79 (2018), pp. 1172–1180, https://doi.org/10.1002/mrm.26748.

[27] Y. Kee, Z. Liu, L. Zhou, A. Dimov, J. Cho, L. de Rochefort, J. K. Seo, and Y. Wang, *Quantitative susceptibility mapping (QSM) algorithms: Mathematical rationale and computational implementations*, IEEE Trans. Biomed. Engrg., 64 (2017), pp. 2531–2545, https://doi.org/10.1109/TBME.2017.2749298.

[28] J. Klohs, A. Deistung, F. Schweser, J. Grandjean, M. Dominietto, C. Waschkies, R. M. Nitsch, I. Knuesel, J. R. Reichenbach, and M. Rudin, *Detection of cerebral microbleeds with quantitative susceptibility mapping in the ArcAbeta mouse model of cerebral amyloidosis*, J. Cerebr. Blood F. Met., 31 (2011), pp. 2282–2292, https://doi.org/10.1038/jcbfm.2011.118.

[29] B. Kressler, L. de Rochefort, T. Liu, P. Spincemaille, J. Quan, and Y. Wang, *Nonlinear regularization for per voxel estimation of magnetic susceptibility distributions from MRI field maps*, IEEE Trans. Med. Imag., 29 (2010), pp. 273–281, https://doi.org/10.1109/TMI.2009.2023787.

[30] W. Li, A. V. Avram, B. Wu, X. Xiao, and C. Liu, *Integrated Laplacian-based phase unwrapping and background phase removal for quantitative susceptibility mapping*, NMR Biomed., 27 (2014), pp. 219–227, https://doi.org/10.1002/nbm.3056.

[31] T. Liu, I. Khalidov, L. de Rochefort, P. Spincemaille, J. Liu, A. J. Tsiouris, and Y. Wang, *A novel background field removal method for MRI using projection onto dipole fields (PDF)*, NMR Biomed., 24 (2011), pp. 1129–1136, https://doi.org/10.1002/nbm.1670.

[32] T. Liu, J. Liu, L. de Rochefort, P. Spincemaille, I. Khalidov, J. R. Ledoux, and Y. Wang, *Morphology enabled dipole inversion (MEDI) from a single-angle acquisition: Comparison with COSMOS in human brain imaging*, Magn. Reson. Med., 66 (2011), pp. 777–783, https://doi.org/10.1002/mrm.22816.

[33] T. Liu, P. Spincemaille, L. de Rochefort, B. Kressler, and Y. Wang, *Calculation of susceptibility through multiple orientation sampling (COSMOS): A method for conditioning the inverse problem from measured magnetic field map to susceptibility source image in MRI*, Magn. Reson. Med., 61 (2009), pp. 196–204, https://doi.org/10.1002/mrm.21828.

[34] T. Liu, P. Spincemaille, L. de Rochefort, R. Wong, M. Prince, and Y. Wang, *Unambiguous identification of superparamagnetic iron oxide particles through quantitative susceptibility mapping of the nonlinear response to magnetic fields*, Magn. Reson. Imaging, 28 (2010), pp. 1383–1389, https://doi.org/10.1016/j.mri.2010.06.011.

[35] T. Liu, C. Wisnieff, M. Lou, W. Chen, P. Spincemaille, and Y. Wang, *Nonlinear formulation of the magnetic field to source relationship for robust quantitative susceptibility mapping*, Magn. Reson. Med., 69 (2013), pp. 467–476, https://doi.org/10.1002/mrm.24272.

[36] Z. Liu, P. Spincemaille, Y. Yao, Y. Zhang, and Y. Wang, *MEDI+0: Morphology enabled dipole inversion with automatic uniform cerebrospinal fluid zero reference for quantitative susceptibility mapping*, Magn. Reson. Med., 79 (2017), pp. 2795–2803, https://doi.org/10.1002/mrm.26946.

[37] S. Mallat, *A Wavelet Tour of Signal Processing: The Sparse Way*, 3rd ed., Academic Press, Burlington, MA, 2008.

[38] C. Milovic, B. Bilgic, B. Zhao, J. Acosta-Cabronero, and C. Tejos, *Fast nonlinear susceptibility inversion with variational regularization*, Magn. Reson. Med., 80 (2018), pp. 814–821, https://doi.org/10.1002/mrm.27073.

[39] F. Natterer, *Image reconstruction in quantitative susceptibility mapping*, SIAM J. Imaging Sci., 9 (2016), pp. 1127–1131, https://doi.org/10.1137/16M1064878.

[40] B. Palacios, G. Uhlmann, and Y. Wang, *Reducing streaking artifacts in quantitative susceptibility mapping*, SIAM J. Imaging Sci., 10 (2017), pp. 1921–1934, https://doi.org/10.1137/16M1096475.

[41] A. Ron and Z. Shen, *Affine systems in $L_2(\mathbf{R}^d)$: The analysis of the analysis operator*, J. Funct. Anal., 148 (1997), pp. 408–447, https://doi.org/10.1006/jfan.1996.3079.

[42] L. I. Rudin, S. Osher, and E. Fatemi, *Nonlinear total variation based noise removal algorithms*, Phys. D, 60 (1992), pp. 259–268, https://doi.org/10.1016/0167-2789(92)90242-F.

[43] F. Schweser, A. Deistung, B. W. Lehr, and J. R. Reichenbach, *Differentiation between diamagnetic and paramagnetic cerebral lesions based on magnetic susceptibility mapping*, Med. Phys., 37 (2010), pp. 5165–5178, https://doi.org/10.1118/1.3481505.

[44] F. Schweser, A. Deistung, and J. R. Reichenbach, *Foundations of MRI phase imaging and processing for Quantitative Susceptibility Mapping (QSM)*, Z. Medizinische Phys., 26 (2016), pp. 6–34, https://doi.org/10.1016/j.zemedi.2015.10.002.

[45] J. K. Seo, E. J. Woo, U. Katscher, and Y. Wang, *Electro-Magnetic Tissue Properties MRI*, 1st ed., Imperial College Press, London, 2014.

[46] Z. Shen, *Wavelet frames and image restorations*, in Proceedings of the International Congress of Mathematicians. Volume IV, Hindustan Book Agency, New Delhi, 2010, pp. 2834–2863.

[47] K. Shmueli, J. A. de Zwart, P. van Gelderen, T. Li, S. J. Dodd, and J. H. Duyn, *Magnetic susceptibility mapping of brain tissue in vivo using MRI phase data*, Magn. Reson. Med., 62 (2009), pp. 1510–1522, https://doi.org/10.1002/mrm.22135.

[48] E. M. Stein and R. Shakarchi, *Functional Analysis. Introduction to Further Topics in Analysis*, Princeton Lect. Anal. 4, Princeton University Press, Princeton, NJ, 2011.

[49] J. Tang, S. Liu, J. Neelavalli, Y. C. N. Cheng, S. Buch, and E. M. Haacke, *Improving susceptibility mapping using a threshold-based* $\boldsymbol{k}$*-space/image domain iterative reconstruction approach*, Magn. Reson. Med., 69 (2013), pp. 1396–1407, https://doi.org/10.1002/mrm.24384.

[50] J. M. G. van Bergen, J. Hua, P. G. Unschuld, I. A. L. Lim, C. K. Jones, R. L. Margolis, C. A. Ross, P. C. M. van Zijl, and X. Li, *Quantitative susceptibility mapping suggests altered brain iron in premanifest Huntington disease*, Amer. J. Neuroradiol, 37 (2016), pp. 789–796, https://doi.org/10.3174/ajnr.A4617.

[51] S. Wang, T. Liu, W. Chen, P. Spincemaille, C. Wisnieff, A. J. Tsiouris, W. Zhu, C. Pan, L. Zhao, and Y. Wang, *Noise effects in various quantitative susceptibility mapping methods*, IEEE Trans. Biomed. Engrg., 60 (2013), pp. 3441–3448, https://doi.org/10.1109/TBME.2013.2266795.

[52] Y. Wang and T. Liu, *Quantitative susceptibility mapping (QSM): Decoding MRI data for a tissue magnetic biomarker*, Magn. Reson. Med., 73 (2015), pp. 82–101, https://doi.org/10.1002/mrm.25358.

[53] Z. Wang, A. C. Bovik, H. R. Sheikh, and E. P. Simoncelli, *Image quality assessment: From error visibility to structural similarity*, IEEE Trans. Image Process., 13 (2004), pp. 600–612, https://doi.org/10.1109/TIP.2003.819861.

[54] C. Wisnieff, T. Liu, P. Spincemaille, S. Wang, D. Zhou, and Y. Wang, *Magnetic susceptibility anisotropy: Cylindrical symmetry from macroscopically ordered anisotropic molecules and accuracy of MRI measurements using few orientations*, NeuroImage, 70 (2013), pp. 363–376, https://doi.org/10.1016/j.neuroimage.2012.12.050.

[55] F. Yanez, A. Fan, B. Bilgic, C. Milovic, E. Adalsteinsson, and P. Irarrazaval, *Quantitative susceptibility map reconstruction via a total generalized variation regularization*, in 2013 International Workshop on Pattern Recognition in Neuroimaging, 2013, pp. 203–206, https://doi.org/10.1109/PRNI.2013.59.

[56] H. Zhang, B. Dong, and B. Liu, *A reweighted joint spatial-Radon domain CT image reconstruction model for metal artifact reduction*, SIAM J. Imaging Sci., 11 (2018), pp. 707–733, https://doi.org/10.1137/17M1140212.

[57] D. Zhou, T. Liu, P. Spincemaille, and Y. Wang, *Background field removal by solving the Laplacian boundary value problem*, NMR Biomed., 27 (2014), pp. 312–319, https://doi.org/10.1002/nbm.3064.